UNIVERSITY OF
BIRMINGHAM

Characterisation of Plasma Arc Technology Processed Waste Products

By

Jishen Mao

A thesis submitted to
The University of Birmingham
For the degree of
Master of Research (MRes)

Department of Metallurgy and Materials
The University of Birmingham
August 2011

ABSTRCT

Plasma arc technology is a novel method that widely applied in industry for the hazardous waste vitrification. After the plasma arc process, the wastes are transformed into inert and glassy materials ready for storage or other applications.

The aim of this project is to characterise a plasma arc processed waste product. Two types of samples were characterised in this study, Sample A is sodium-free and Sample B is sodium-contained. The microstructure of the samples was characterised using XRD, SEM and TEM; mechanical properties of the samples were measured including Vickers hardness and compressive strength; dissolution of the samples in alkaline solution was measured to test the chemical stability. XRD results show that both of the samples are amorphous, which is confirmed by the TEM electron diffraction study. The sodium-free sample contains areas in green color and areas in white color, while the sodium-contained sample is all in green. SEM results show that the green area in sodium-free sample has homogenous structure and the white area has a dendrite-like structure. The bright part in the dendrite-like structure contains more Al, Si, Ce but less Mg than the dark part. A black fiber-like structure can be found in the sodium-contained sample. The fiber-like structure contains more O, Mg, Al but less Si than the rest of the sample. A detail study of electron diffraction in TEM was performed by transforming the electron diffraction patterns into reduced density function G(r) (RDF). The results show that the nearest-neighbor distance in sodium-contained sample is larger than the sodium-free sample.

Mechanical property measurements show that the sodium-free sample has higher Vickers hardness and compressive strength values than the sodium-contained sample. The sodium-free sample also has a higher dissolution rate than the sodium-contained sample as indicated in the chemical stability study.

ACKONWLEGMENTS

First I would like to sincerely thank my supervisor Dr. Yulung Chiu for his advice and support throughout my study. I attribute the level of my Master degree to his encouragement and effort, without him this thesis would not have been completed. I would also like to thank Professor Ian Jones for his help and encouragement during the whole period of my Master project.

I would like to thank Dr. Ding for his help and suggestion with my thesis writing. I would also like to thank Dr. Yauyau Tse for her help with my XRD study. In addition, I would like to thank Dr. Ming Chu for her help with my TEM training.

I would like to thank Paul and Theresa in Electron Microscopy Center for the help with my SEM trainings. Thanks are also given to Shadi and Xiaoning for the help with XRD operation. Thanks are also gone to Wei Li and Dave for the help with the mechanical properties tests.

I would like to thank my colleagues Winson and Anqi for the suggestion with my thesis writing. I would also like to thank my colleagues Thiago, Ruilin, Xinxin and others for the help during my Master study.

Special thanks are given to Tetronics Ltd for providing the samples used in my project.

Last I would like to thank to my family and my girlfriend Miffy for their love and support which are so much important for me during the whole period of my Master study.

CONTENTS

CHAPTER THREE: Experimental Procedures.

CHAPTER FOUR: Results and Discussion.

CHAPTER ONE

INTRODUCTION

The increase of population, consumerism and the evolution of technology and industry are some of the causes for the worldwide rise in the generation of hazardous waste. Nowadays various processes such as melting, incineration, pyrolys and vitrification can be carried out for the treatment of the wastes. The aim of these treatments is to destroy the organic fraction and convert the inorganic fraction into an inert slug or glass that can be reused or harmlessly disposed of in landfills [1, 2, 3].

A novel method for vitrification called plasma arc technology is recently widely applied in industry for the treatment of hazardous waste materials. Plasma arc has advantages such as high temperature, high intensity, non-ionising radiation and high energy density [4]. Stabilization of the waste and a significant volume reduction can be achieved using this technology; this makes the process particularly attractive for nuclear waste treatment [5]. After the plasma arc process, waste products have been transformed into vitrified slugs and can be classified as inert waste and become acceptable for landfills or other applications. Granulated slugs could be reused for roadbed or concrete aggregates while cast slug can also be reused for interlocking blocks, tiles and bricks [4].

Currently there is an interest from industry to understand the mechanical properties of plasma arc technology processed waste products, which are typically glassy materials. To explore the potential applications of this type of material, characterisation of the products needs to be carried out. In this project, microstructure characterization, mechanical properties and chemical stability tests of the glassy material are carried out. The techniques involved in this study include X-ray Diffractometry (XRD), Scanning Electron Microscopy (SEM), Transmission Electron Microscopy (TEM), Vickers hardness test, compression test and dissolution test in alkaline solutions.

References

[1] P. Colombo, G. Brustain, E. Bernardo, G. Scarinci, Curr. Opin. Solid State Mater. Sci. 7 (2003) 225-239.

[2] T. Sabbas, A. Polettini, R. Pomi, T. Astrup, O. Higlmar, P. Mostbauer, G. Cappai, G. Magel, S. Salhofer, C. Speiser, S. Heuss-Assbichler, R. Klein, P. Lechner, Waste Manage. 23 (2003) 61-88.

[3] Y. M. Guo, T. C. Lin, P. J. Tsai, J. Hazard. Mater. 133 (2006) 75-78.

[4] E. Gomez, D. Amutha Rani, C. R. Cheeseman, D. Deegan, M. Wise, A. R. Boccaccini, J. Hazard. Mater. 161 (2009) 614-626.

[5] D. Deegan, C. Scales, Proc. 11th Int. Conference on Environmental Remediation and Radioactive Waste Management (2007) ICEM07-7271.

CHAPTER TWO

LITERATURE REVIEW

2.1 Radioactive Waste and Its Disposal

2.1.1 Introduction to Radioactive Waste

Radioactive waste can be defined as a material that contains or is contaminated by radionuclides. In addition, the radionuclides in radioactive waste should at concentrations greater than the exempted quantities which established by the competent authorities [1]. Radioactive waste usually generates from the production of nuclear energy and from the use of radioactive materials in industrial applications, research and medicine.

Generally radioactive waste can be divided into five categories: very low-level waste (VLLW) which can be safely disposed of with ordinary refuse; low-level waste (LLW) which primarily contains low concentration beta or gamma contamination, and may include alpha contaminated material; intermediate level waste (ILW) which contains higher concentrations of beta or gamma contamination and sometimes alpha emitters; high-level waste (HLW) which contains high concentrations of beta or gamma emitting fission products and alpha emitting actinides. Among all the five radioactive waste types LLW is the majority [2].

As the rapid increase in the nuclear industry, more and more radioactive waste was generated. Due to the hazardous nature of radioactive waste that may emit ionizing radiation and cause environmental problems, apparently there has been an increasing emphasis on the importance of the disposal of the radioactive waste for the protection of human health and the environment, that means to produce a safe and quality end product for all disposed radioactive wastes. This goal is achievable by obtaining an accurate and thorough assessment of the physical, chemical and radiological characterisation of the radioactive waste [3].

2.1.2 Radioactive Waste Disposal

2.1.2.1 Introduction to Process Methods

Due to the hazardous nature of the radioactive waste, sophisticated process methods are required to successfully isolate it from interacting with the environment. And there treatments are followed by a long-term management strategy involve storage, disposal or transformation of the waste into a non-toxic form [4]. Three process methods include vitrification method; ion exchange method and synroc method are introduced in this section.

One way to achieve the stabilization of the waste for long-term storage is through vitrification method [5]. Firstly the waste is mixed with sugar and then passed through a heated tube to evaporate the water from the waste, this is called calcination. Then the calcine is fed continuously into an induction heated furnace with fragmented glass, the melt product is then poured into steel cylinders and when it cooled, the fluid vitrifies into the glass. The resulting glass of this method is a new substance and the waste products are bonded into the glass matrix when it solidifies. In this form, the waste products are expected to be immobilized for a long period of time.

Ion exchange method [6] is another widely used way in radioactive waste disposal. It is often applied for medium active wastes in nuclear industry and the purpose is to concentrate the radioactivity into a small volume. The treated radioactive bulk becomes much less in volume and then discharged. One example of this method is using a ferric hydroxide floc to remove radioactive metals from aqueous mixtures. The resulting sludge can be placed in a metal drum before mixed with cement to form a solid waste because the radioisotopes are absorbed onto the ferric hydroxide during the process.

A more sophisticated and novel way to immobilize radioactive waste is called synroc which originated from Australia (T. Ringwood, et al.). Currently it is mainly applied for military use but may come into commercial use for civil wastes. The advantage of this technique is that it provides effective and durable means of immobilizing various forms of high-level radioactive wastes for disposal. It is basically a ceramic made from several natural minerals which together incorporate into their crystal structures nearly all of the elements present in high level radioactive waste. Synroc can take various forms depending on its specific use and can be tailored to immobilize particular components in the HLW.

2.1.2.2 Plasma Arc Process Technology

Recently an advanced technique for the vitrification of radioactive wastes called plasma arc technology is widely used. The advantages of this technique include high interaction temperature, high intensity, non-ionising radiation and high energy density [7]. It offers unique advantages for the treatment of radioactive waste such as minimal environmental impact being a clean process, minimised off-gas volumes and secondary waste streams, high radionuclide incorporation rates, a stable and low volume final waste-form for a wide range of applications [8].

This process is a non-incineration thermal process and extremely high temperatures are used in an oxygen-starved environment to completely decompose the input waste material into very simple molecules. The intense and versatile heat generation capabilities of plasma technology enable it to treat radioactive waste in a safe and reliable manner. The by-products of the process are a combustible gas and an inert slag. It also exhibits much lower environmental levels for both air emissions and slag leachate toxicity than other thermal technologies. The core of the plasma arc process is converting the raw materials (or waste stimulates) into a glass form which is capable of being continuously fed into a sealed furnace, and then heated in a controlled environment by a plasma arc created by plasma torches, a twin electrode DC plasma arc facility is shown in Figure 2.1 [9]. Once the process starts, a copper crucible is used to contain the melt, a twin electrode plasma system was used as the heat source and a calcium aluminosilicate slag (CAS) is used as the host receptor of the raw materials. After the reaction finished, the final waste-form was allowed to solidify and then removed from the furnace, a significant volume reduction of the feed material is achieved through the process. Figure 2.2 shows the molten and solidified slag, respectively [9]. The main plasma operating variables are plasma power, oxidant type (steam and oxygen) and addition rate [10].

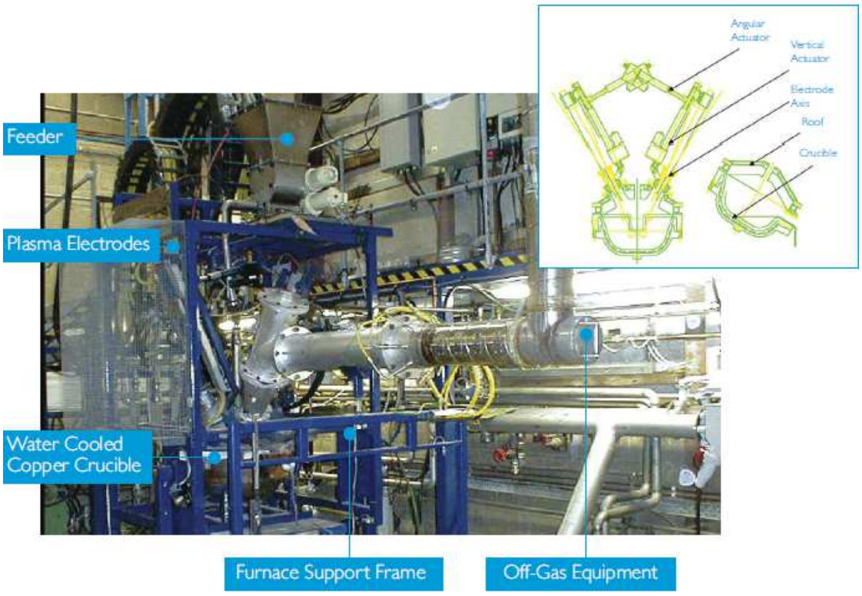

Figure 2.1: photograph of a twin electrode DC plasma arc facility [9].

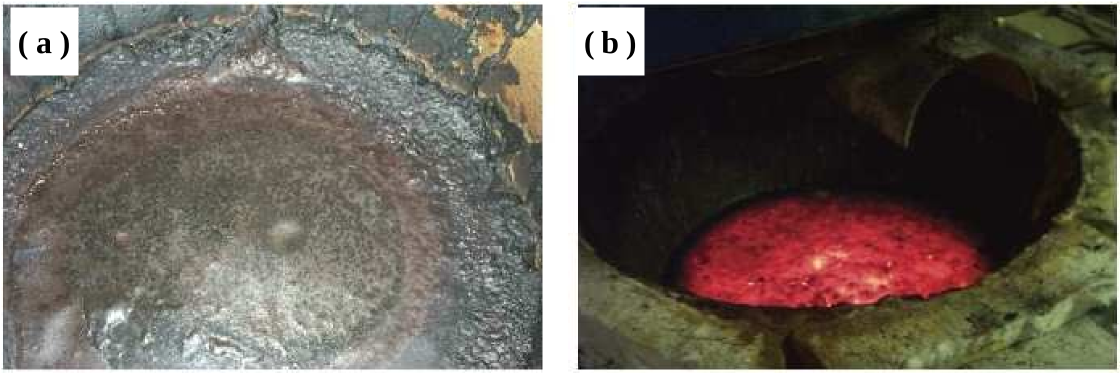

Figure 2.2: images showing solidified slag (a) and molten slag (b) [9].

2.2 Characterisation of the Waste Products

Characterisation of the processed waste products plays a vital role in the hazardous waste disposal. For safety reasons the chemical properties of the waste products need be assessed. Furthermore, the mechanical properties, thermal properties and microstructure information can also be obtained during the characterisation, which may suggest some potential applications of the wastes products.

2.2.1 Introduction to Characterization Methods

To characterise the processed waste products usually refers to the characterisation of the mechanical properties, thermal properties and chemical properties of the products. This is achievable by using various characterisation techniques. Mechanical properties of the waste product can be measured and obtained such as micro-hardness, Young’s modulus, flexural strength and compressive strength. These properties may be related to the microstructure of the waste products; therefore, the microstructural information of the products also needs to be studied. Generally, electron microscopes include Optical Microscopy (OM), Scanning Electron Microscopy (SEM) and Transmission Electron Microscopy (TEM) are very powerful tools to study and give the microstructure information of the product, moreover, X-ray Diffractometry (XRD) and energy dispersive X-ray analysis (EDX) which is usually combined with a SEM or TEM can be used to identify its phase composition. Another method called differential thermal analysis (DTA) is usually used to study the thermal evolution of the waste products. An important property of the glassy waste product is its chemical durability, to access to it, long-term leaching test can be performed. After observing the initial leach ratio of glass components in the waste products, the leaching mechanism can be studied. The chemical stability of the waste products is usually studied by measuring the dissolution rate of the waste products in aqueous solutions with different PH (acid or alkaline) or with different temperatures. The release of a specific element in solutions from the waste products can be also studied.

2.2.2 Characterisation of Glassy and Amorphous Waste Products

Studies of glassy and amorphous waste products processed by plasma vitrification were carried out by previous researchers and some of the characterisation results are presented in this section.

J. A. Roether and his colleagues [11] reported on the use of plasma vitrification for the treatment of air pollution control residues and the properties of sintered glassy materials obtained was characterised. In this process, the waste was blended with silica and alumina and then melted using DC plasma arc. The glass produced was then crushed, milled, uni-axially pressed and sintered at different temperatures between 750 and 1150 °C, and the glassy products were investigated using XRD, SEM and TEM. Vickers hardness, flexural strength, Young's modulus and thermal shock resistance of the products were also assessed. The results showed that the mechanical properties of the products were comparable to or superior to natural materials such as granite and marble, and commercial material such as Macor^{TM}. These wastes derived materials could find application in the construction sector. The thermal shock resistance of the products was also high compared to other glass materials, which implies potential for application as a refractory or as a matrix for high temperature composite materials. The improved mechanical properties and thermal shock resistance may be related to the existence of a dual glass-crystalline microstructure which is confirmed by the TEM results.

C. P. Yoganand and his group [12] reported the characterisation of a $CaO-MgO-SiO_2$ glass ceramic synthesised using a transferred arc plasma (TAP) processing method. Homogeneous mixture of 51.6% SiO_2, 35.6% CaO and 12.8% MgO was kept in the anode well of the TAP torch. Then the melt was cooled to solidify by applying forced air on it. Different process time of the synthesis was set up to check its influence on the produced glass ceramics. The results of XRD experiment showed a trend that the crystallinity of the glass ceramics was higher for longer process time. Also for longer process time, the presence of induced devitrification in the synthesised materials was confirmed by SEM observation. It may be concluded that a longer processing time is beneficial for the production of glass ceramic with higher crystalline phases and devitrified microstructure.

A. Lopez-Delgado and his colleagues [13] studied the vitrification of a solid waste coming from the secondary aluminum industry at 1500 °C. This solid waste was considered hazardous because it can generate gases such H_2, NH_3 and CH_4 in the presence of waster or moisture. Silica sand and calcium carbonate were added as external raw materials for the glass formation. Different glass compositions with Al_2O_3 ranging between 20% and 54% were studied. The results showed that vitrification was a suitable immobilisation procedure for an aluminum-rich waste because it allowed the successful immobilisation of high proportions of the aforementioned waste. In addition, the values of Vickers hardness and toughness obtained were comparable to those reported for calcium aluminosilicate glasses. Only glasses with high CaO/Al_2O_3 ratio and low SiO_2 content were susceptible to chemical attack with boiling water.

2.3 Electron Diffraction of Amorphous Materials

2.3.1 Introduction to Electron Diffraction in Studying Amorphous Materials

Electron diffraction is a powerful analytical tool for investigating the structure of materials. Nowadays with the significant improvements of the apparatus used to perform electron diffraction, the accuracy and speed of the electron diffraction measurements also increase as well as the extension on the range of its applications. Electron diffraction can be used to study different kinds of materials include gases, crystals, polycrystalline and amorphous solid [14]. The aim of this section is to explain the basic theory of electron diffraction in amorphous materials.

Amorphous material can be defined as an aggregation of atoms where the locations of the neighboring atoms are defined by a probability function such that the probabilities are never unity [14]. The position of a neighboring atom in an amorphous material is on a scale of about 0-10 Å. This means amorphous material still exhibits a degree of order oat 0-10Å scale and this order is called short range order (SRO). Electron diffraction has been proved to be a useful tool for quantifying SRO in amorphous materials [15, 16]. Using the pair correlation function [17] it is possible to obtain the average SRO structural information from electron diffraction. However, pair correlation function only gives a limited description of the structure of amorphous materials as it is a one-dimensional average of a three-dimensional structure. For this reason new electron diffraction techniques have been developed to obtain a better description of amorphous materials. For example, a possible way to achieve more amorphous structural information is to combine electron diffraction and electron imaging. The images provide two-dimensional structural information as reported by Howie and Rudee [18, 19] and Gibson and Treacy [20]. Another method reported by Howie [21] is to measured the correlations from micro-diffraction patterns formed using a scanning transmission electron microscopy (STEM). By using STEM, a very small volume of the amorphous material can be investigated [22]. Although there are still limitations associated with it, electron diffraction has been proven very successful by giving the structural complexity of amorphous materials. In a word, electron diffraction is a vital tool in the study of amorphous material.

2.3.2 Electron Diffraction in Transmission Electron Microscopy (TEM)

The study of the structure of amorphous material usually starts with the collecting of scattering data to large scattering angles and converts the data into information about atomic spatial relationships. The scattering data can be obtained using either electrons, X-rays or neutrons. However, due to the small cross section of electrons scattering when compared with X-rays or neutrons, electron diffraction has unique advantage in studying thin film materials.

Modern TEM offers a convenient environment for performing electron scattering experiments. The fine control of high energy (100 keV - 400 keV) electron beam allows performing accuracy diffraction experiments, the easy specimen change makes it possible to examine a number of different specimens in a short period of time, the combination with other spectrometers such as energy dispersive X-rays spectrometer (EDX) [23] and electron energy loss spectrometer (EELS) [24, 25] increases the total information of the microstructure of specimens that can be obtained.

Cockayne and McKenzie [26] have developed a technique which couples a TEM with an electron energy loss spectrometer (EELS) [27] in order to make particularly sensitive measurements of electron diffraction patterns. Radial Distribution Function (RDF) analysis was then performed on the elastically scattered component of these measurements to obtain information about the atomic structure of materials. Thus the calculation of a radial distribution curve is the logical first step in the analysis of an electron diffraction pattern [28].

The electron scattering data in a TEM can be obtained directly, however, the interpretation of data can be accomplished only if a full understanding of how the high energy electron beam interacts with an amorphous material is made. What makes this problem more complex is that the electron can interact with materials in a variety of ways which provide different detectable signals including backscattered electrons, auger electrons and elastically and inelastically scattered electrons. However, among all these signals the elastically scattered electron can be used to determine the atomic structure of amorphous material more readily. The primary mechanism of the elastic scattering of electron is the Coulombic interaction between the electron and the atom.

An elastic scattering event can be defined as a collision in which the kinetic energy is conserved [29], When an electron is elastically scattered by an atom, due to the large difference between the masses of the particles, the electron suffers a change in momentum but its kinetic energy will be conserved. As a consequence of the fact that electrons have a wave-like nature, de Broglie postulated that elastically scattered electrons exhibit coherency [30]. Here coherency described how the phases of different electron waves are related. For elastically scattered electrons the degree of coherency decreases as the scattering angle increases, so low angle elastic scattering (i.e. angles less than 4°) in TEM is highly coherent and gives rise to diffraction phenomena which can be used to obtain structural information of amorphous materials.

2.3.3 Elastic Scattering Theory

The elastic scattering of an electron by an atom is a time dependent process in what at time t_1 the electron is far away from the atom and there's no interaction between them; at time t_2 the electron is close enough to interact with the atom and the electron is scattered by the atom; at time t_3 the electron and atom are again far apart and no interaction happens between them.

According to quantum mechanics [31], this time-dependent process can be reformulated as a stationary state which is an eigenstate of the Hamiltonian, or in other words, a state of definite energy so that it can be considered to be time independent. In this case, the Time Independent Schrödinger Equation (TISE) [32] can be solved to determine the wavefunction ψ which is a function typically of space or momentum and possibly of time that returns the probability amplitude of a position or momentum of an electron. Here probability amplitude is a complex number whose modulus square represents a probability or probability density. One thing should be noticed here that in the following derivation of ψ, individual components of ψ are referred to as the state of the electron before and after scattering although the whole scattering process is being treated independently of time, this is not so strictly correct but makes the derivation more convenient.

2.3.3.1 Scattering from a Single Atom

The electron is described by wavefunction $\psi(\mathbf{r}, t)$ and as previously mentioned the electron interacts through Coulombic forces with the electrostatic potential of the atom, $V(\mathbf{r}, t)$. Schrödinger equation describes such an interaction:

$$\frac{-\hbar^2}{2m}\nabla^2\psi(\mathbf{r},t) + V(\mathbf{r},t)\psi(\mathbf{r},t) = i\hbar\frac{\partial}{\partial t}\psi(\mathbf{r},t) \qquad \textbf{(2.1)}$$

where $\frac{-\hbar^2}{2m}\nabla^2$ is the kinetic energy operator and m is the mass of electron, ħ is Planck's constant divided by 2π and ∇^2 is the Laplace differential operator $\nabla^2 = \frac{\partial^2}{\partial x} + \frac{\partial^2}{\partial y} + \frac{\partial^2}{\partial z}$ where x, y, z are the Cartesian coordinates of space, $\psi(\mathbf{r}, t)$ is the probability amplitude for the electron to be found at position r at time t.

If the time variation of $V(\mathbf{r}, t)$ is slow when compared to $\psi(\mathbf{r}, t)$, it may assume that $V(\mathbf{r},t) = V(\mathbf{r})$, also $\psi(\mathbf{r}, t)$ can be separated into two parts include a space term and a time term [34]:

$$\psi(\mathbf{r},t) = \psi(\mathbf{r})e^{-iEt/\hbar} \qquad \textbf{(2.2)}$$

where $E = \hbar\omega$ is the energy of the electron, $\omega = 2\pi\gamma$ where γ is frequency. Then make substitution and Eqn. (2.1) can be written as:

$$[\nabla^2 + \frac{2m}{\hbar^2}(E - V(\mathbf{r}))]\psi(\mathbf{r}) = 0. \qquad \textbf{(2.3)}$$

Eqn. (2.3) is the TISE for the scattering of an electron by an atom. To solve this TISE the derivation can be simplified by considering the solutions to the TISE at position **r**, before and after the scattering event, separately. The solution before the scattering event describes the incident electron beam, $\psi_{inc}(\mathbf{r})$, whereas the one after the event describes the scattered electron beam, $\psi_{scatt}(\mathbf{r})$.

For $\psi_{inc}(r)$, $V(\mathbf{r})=0$ because before the scattering event the electron is moving in free space, and the TISE can be written as:

$$[\nabla^2 + \frac{2m}{\hbar^2}E]\psi_{inc}(\mathbf{r}) = 0. \qquad \textbf{(2.4)}$$

Solving this equation for $\psi_{\mathrm{inc}}(\mathrm{r})$ gives:

$$\psi_{\mathrm{inc}}(\mathbf{r}) = \mathrm{e}^{\mathbf{ik.r}}. \qquad \textbf{(2.5)}$$

Eqn. (2.5) describes a plane wave [33] of unit amplitude and wave vector $\mathbf{k}$, where $|\mathbf{k}| = \frac{2\pi}{\lambda}$ where λ is the wavelength of the electron.

For $\psi_{\mathrm{scatt}}(\mathbf{r})$, $\mathrm{V}(\mathbf{r})$ also equals to zero and after the scattering event, to a distance observer, the atom appears to be an electron wave source, emitting electron waves into free space [34]. The TISE can then be written as:

$$[\nabla^2 + \frac{2\mathrm{m}}{\hbar^2}\mathrm{E}]\psi_{\mathrm{scatt}}(\mathbf{r}) = \rho(\mathbf{r}) \qquad \textbf{(2.6)}$$

where $\rho(\mathbf{r})$ represents the electron wave source.

To solve Eqn. (2.6) one assumption is introduced, for the moment, the electron wave source is a point source and consequently $\rho(\mathbf{r})$ can be represented by a delta function (i.e $\rho(\mathbf{r}) = \mathrm{B}.\delta(\mathbf{r} - \mathbf{r}')$ where B is the strength of the source) [16]. Using this assumption, the solution to the TISE is:

$$\psi_{\mathrm{sph}}(\mathbf{r}) = (\frac{\mathrm{B}}{4\pi})\frac{\mathrm{e}^{\mathbf{i}\mathbf{k}'|\mathbf{r}-\mathbf{r}'|}}{|\mathbf{r}-\mathbf{r}'|} \qquad \textbf{(2.7)}$$

Eqn. (2.7) is a spherical wave [34] centered on the source which decreases in amplitude as the radial distance from the source $|\mathbf{r} - \mathbf{r}'|$ increases.

Then another assumption is made that the atomic potential, $\mathrm{V}(\mathbf{r})$, can be represented by a finite distribution of point sources and that the strength of each point source is given by the interaction between $\mathrm{V}(\mathbf{r})$ and $\psi(\mathbf{r})$, that is $\mathrm{B} = \mathrm{B}(\mathbf{r}) = \mathrm{V}(\mathbf{r})\psi(\mathbf{r})$ [16] (shown in Figure 2.3). In this case $\psi_{\mathrm{scatt}}(\mathbf{r})$ is then the superposition of the spherical waves, $\psi_{\mathrm{sph}}(\mathbf{r})$, scattered from each of the individual point sources [16]:

$$\psi_{\mathrm{scatt}}(\mathbf{r}) = \frac{1}{4\pi}\int_0^\infty V(\mathbf{r}')\,\psi(\mathbf{r}')\frac{e^{ik'|\mathbf{r}-\mathbf{r}'|}}{|\mathbf{r}-\mathbf{r}'|}d\mathbf{r}'. \tag{2.8}$$

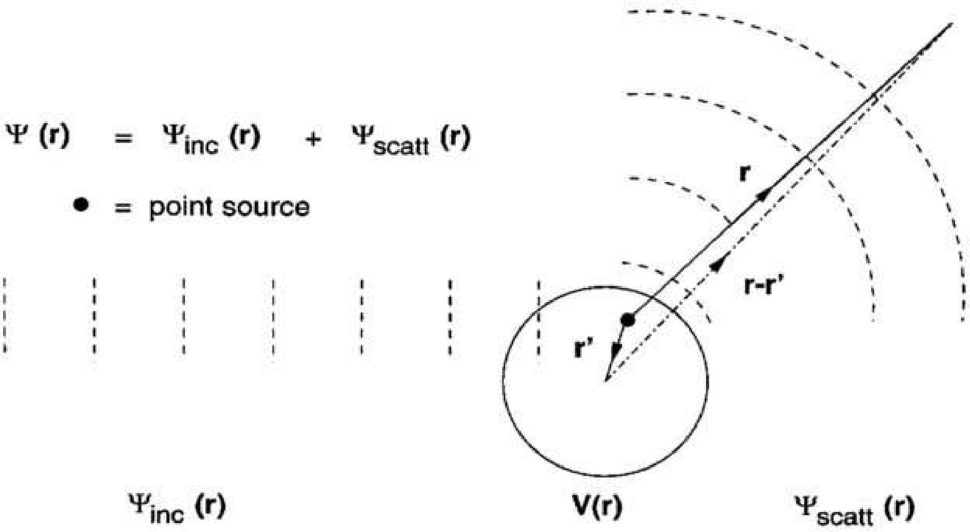

Figure 2.3 [16]: diagram showing the scattering of a planar electron wave by an atom.

Then combine the solutions for $\psi_{\mathrm{inc}}(\mathbf{r})$ and $\psi_{\mathrm{scatt}}(\mathbf{r})$ into an expression for $\psi(\mathbf{r})$ gives

$$\psi(\mathbf{r}) = e^{i\mathbf{k}.\mathbf{r}} + \frac{1}{4\pi}\int_0^\infty V(\mathbf{r}')\,\psi(\mathbf{r}')\frac{e^{ik'|\mathbf{r}-\mathbf{r}'|}}{|\mathbf{r}-\mathbf{r}'|}d\mathbf{r}' \tag{2.9}$$

The difficulty to solve Eqn. (2.9) is that the integration term in this equation is itself dependent on the solution through the interaction between ψ(r) and V(r). However, notice that the amplitude of the scattered wave is much smaller than that of the incident wave it can be assumed that ψ(r) in the integral of Eqn. (2.9) can be replaced with $\psi_{\mathrm{inc}}(\mathbf{r})$, this is so called first order Born approximation [35]. When consider a particular case of an electron beam being scattered through a material, it is equivalent to assume that each electron is only scattered once, this situation is known as kinematic scattering. Applying Born approximation to Eqn. (2.9):

$$\psi(\mathbf{r}) = e^{\mathbf{ik.r}} + \frac{1}{4\pi}\int_0^\infty V(\mathbf{r}')\,\psi_{\text{inc}}(\mathbf{r}')\frac{e^{i\mathbf{k}'|\mathbf{r}-\mathbf{r}'|}}{|\mathbf{r}-\mathbf{r}'|}d\mathbf{r}'. \qquad \textbf{(2.10)}$$

The measurements of $|\psi(r)|$ are usually made at large distance from the scattering centre and since $\mathbf{r} \gg \mathbf{r}'$,

$$\frac{e^{i\mathbf{k}'|\mathbf{r}-\mathbf{r}'|}}{|\mathbf{r}-\mathbf{r}'|} \approx \frac{e^{ik'.r}}{r}.\,e^{-i\mathbf{k}'.\mathbf{r}'}$$

and Eqn. (2.10) becomes:

$$\psi(\mathbf{r}) = e^{\mathbf{ik.r}} + \frac{1}{4\pi}\frac{e^{ik'.r}}{r}\int_0^\infty V(\mathbf{r}')\,\psi_{\text{inc}}(\mathbf{r}')e^{-i\mathbf{k}'.\mathbf{r}'}d\mathbf{r}'. \qquad \textbf{(2.11)}$$

Using Eqn. (2.5) and define that $\mathbf{Q} = \mathbf{k} - \mathbf{k}'$, the integral tern in Eqn. (2.11) can then be written as:

$$f(Q) = \int_0^\infty V(\mathbf{r}')\,e^{-i\mathbf{Q}.\mathbf{r}'} \qquad \textbf{(2.12)}$$

where $Q = |\mathbf{Q}|$ and f(Q) is the atomic scattering factor. f(Q) is very useful in the of diffraction because it describes the angular dependence and amplitude of the scattered wave and $|f(Q)|^2$ is proportional to the scattered intensity. Also it is that f(Q) is the Fourier transform of the atomic potential [37, 38] which displays the direct relationship between the intensity and the elastically scattered electrons and the atomic potential. One needs to be noticed here, when use Born approximation to determine f(Q) for heavy atoms errors may be introduced. However, usually this error can be neglected because the effect that the error has is minimal.

2.3.3.2 Scattering from a Unit Cell of Atoms

A unit cell of atoms can be described as, an array of the total N atoms at position $\mathbf{r}_\mathrm{m}$ $(1 \leq \mathrm{m} \leq \mathrm{N})$. The scattering amplitude $\mathrm{F(Q)}$ from a unit cell of atoms is called structure factor and this structure factor can be derived by noting that $\mathrm{F(Q)}$ is the Fourier transform of the atomic potential of the unit cell of atoms [39]. By writing the potential of the m-th atom as $\mathrm{V_m}(\mathbf{r})$ and its position vector as $\mathbf{r}_\mathrm{m}$, and neglecting the effect of the redistribution of valence electrons due to chemical bonding effects, the atomic potential for the unit cell of atoms is given by:

$$\mathrm{V}(\mathbf{r}) = \sum_{\mathrm{m}=1}^{\mathrm{N}} \mathrm{V_m}(\mathbf{r} - \mathbf{r}_\mathrm{m}). \qquad \textbf{(2.13)}$$

And thus the Fourier transform of this potential $\mathrm{V(r)}$ gives the structure factor:

$$\mathrm{F(Q)} = \sum_{\mathrm{m}=1}^{\mathrm{N}} \mathrm{f_m(Q)} e^{\mathbf{i}\mathbf{Q}\cdot\mathbf{r}_\mathrm{m}}. \qquad \textbf{(2.14)}$$

Then notice that $|\mathrm{F(Q)}|^2$ is proportional to the scattered intensity from a unit cell of atoms, the diffraction beam intensity is equal to:

$$\mathrm{I(Q)} = \sum_{\mathrm{m}=1}^{\mathrm{N}} \sum_{\mathrm{n}=1}^{\mathrm{N}} \mathrm{f_m(Q) f_n(Q)} e^{\mathbf{i}\mathbf{Q}\cdot\mathbf{r}_\mathrm{mn}} \qquad \textbf{(2.15)}$$

where $\mathbf{r}_\mathrm{mn} = \mathbf{r}_\mathrm{m} - \mathbf{r}_\mathrm{n}$. Eqn. (2.15) shows that $\mathrm{I(Q)}$ is dependent on the atom type through the atomic scattering factors and the distance separating atom pairs at positions $\mathbf{r}_\mathrm{m}$ and $\mathbf{r}_\mathrm{n}$.

2.3.4 From Diffraction Data to Structure Information

The scattered intensity $\mathrm{I(Q)}$ which is normally obtained in experiment is then Fourier transformed to obtain the information about the atomic structure within the sample from which the diffraction pattern was formed. Amorphous solids are statistically isotropic and can be described by the interatomic distance r and probability distribution. If the vector $\mathbf{r}_{mn} = \mathbf{r}_m - \mathbf{r}_n$ takes all orientations, its terminal point lies anywhere on the surface of a sphere of radius of $\mathbf{r}_{mn}$ [34]. The contribution to the amplitude of scattering from each pair atoms is then given by:

$$e^{i\mathbf{Q}.\mathbf{r}_{mn}} = \frac{1}{4\pi \mathbf{r}_{mn}{}^2} \int_0^{2\pi} dV(\mathbf{r}) \int_0^{\pi} e^{iQ\cos\theta}\, r_{mn}{}^2 \sin\theta\, d\theta = \frac{\sin(Qr_{mn})}{Qr_{mn}}. \tag{2.16}$$

Then add the terms in Eqn. (2.15):

$$I(Q) = \sum_{m=1}^{N} \sum_{n=1}^{N} f_m(Q) f_n(Q) \frac{\sin(Qr_{mn})}{Qr_{mn}}. \tag{2.17}$$

Eqn. (2.17) is the Debye scattering equation, which forms the basis for the radial distribution function (RDF) method first introduced by Pauling and Brockway [34].

2.3.4.1 Single Atomic Species

If the amorphous sample contains only one atomic species, $f_m(Q)$ will be equal to $f_n(Q)$ and the subscripts of f(Q) can be dropped. Then Eqn. (2.15) can be split into self and cross terms occurring when $n = m$ and $n \neq m$. Eqn. (2.15) can then be written as

$$I(Q) = \sum_{m=1}^{N} f(Q)^2 + \sum_{m=1}^{N} f(Q)^2 \sum_{n\neq m}^{N} e^{i\mathbf{Q}.\mathbf{r}_{mn}} \tag{2.18}$$

Here the first term in Eqn. (2.18) $\sum_{m=1}^{N} f(Q)^2$ decreases monotonically as a function of Q, while the second term oscillates about this background. Figure 2.4 shows schematically the distribution of the scattered intensity calculated for a system of N atoms [34]. Now the radial distribution function $J(r) = 4\pi r^2 \rho(r)$ can be introduced and gives the average number of atoms situated on the spherical layer at a distance between r and $r + dr$ from a given atom. Define ρ_a as the average density of atoms in the sample, by adding and subtracting a term involving ρ_a, two integral terms can be obtained and each term extends over the column of the sample:

$$I(Q) = \sum_{m=1}^{N} f(Q)^2 + \sum_{m=1}^{N} f(Q)^2 \int_v \left[\rho(\mathbf{r}_{mn}) - \rho_a\right] e^{i\mathbf{Q}\cdot\mathbf{r}_{mn}} dV_n + \sum_{m=1}^{N} f(Q)^2 \rho_a \int_v e^{i\mathbf{Q}\cdot\mathbf{r}_{mn}} dV_n \quad \textbf{(2.19)}$$

For a fixed separation $\mathbf{r}_{mn} = \mathbf{r}$, the mean density of particles $\rho(\mathbf{r}) = \langle\rho(\mathbf{r}_{mn})\rangle$ is introduced, where the average is taken over all pairs of atoms $\mathbf{r}_{mn}$. If there is no preferred orientation in the sample, the function $\rho(\mathbf{r}) - \rho_a$ is independent of the direction of $\mathbf{r}$ and $\rho(\mathbf{r}) - \rho_a = \rho(r) - \rho_a$. The term involved $\rho(\mathbf{r}_{mn}) - \rho_a$ in Eqn. (2.19) becomes

$$Nf(Q)^2 \int_0^\infty \int_0^\pi [\rho(r) - \rho_a] e^{iQr\cos\theta} 2\,\pi r^2 \sin\theta\, d\theta dr$$
$$= Nf(Q)^2 \int_0^\infty 4\pi r^2 [\rho(r) - \rho_a] \frac{\sin(Qr)}{Qr} dr \quad \textbf{(2.20)}$$

where the range of integration over $\mathbf{r}$ extends from zero to infinity. Then the upper limit of integration is replaced by infinity, if define $g(r) = \rho(r)/\rho_a$, in the case of a non-crystalline material $g(r)$ approaches unity for r greater than a few atomic distance [34] (shown in Figure 2.5), and this scale is many times smaller than the size of the sample. The third term in Eqn. (2.19) which also known as the function $S(Q)$ depends on the shape of the sample and is usually negligible everywhere except for the case of scattering through very small angles [16] (shown in Figure 2.6).

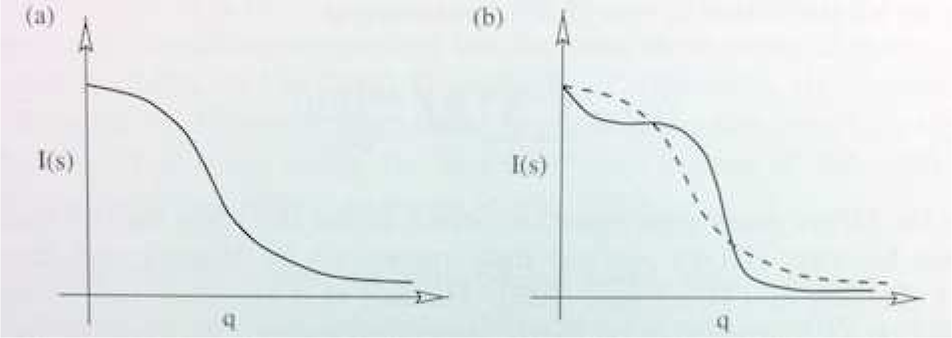

Figure 2.4 [34]: schematically diagrams showing distribution of intensity calculated for (a) uncorrelated and (b) correlated ensembles of atoms.

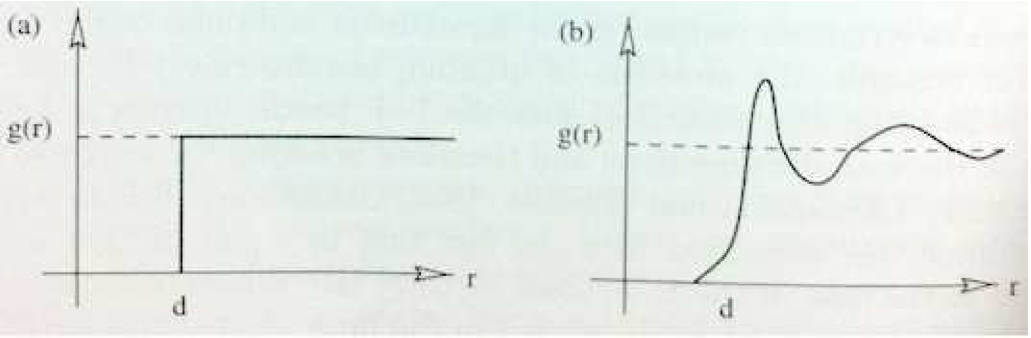

Figure 2.5 [34]: the pair correlation function g(r) for (a) gas and (b) non-crystalline solid, for $r \gg d$ *the function g(r) approaches unity.*

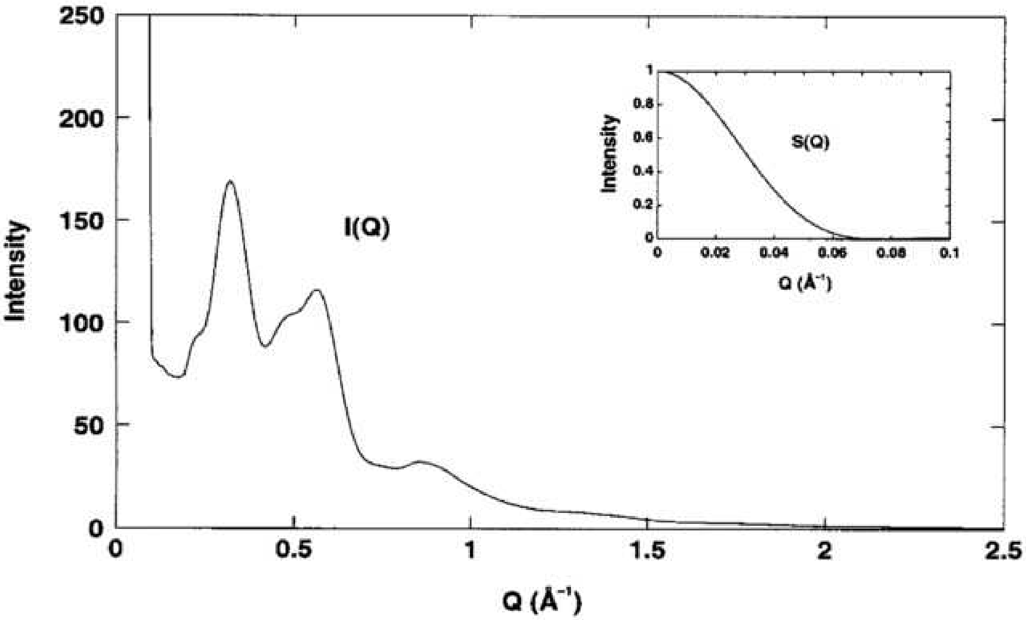

Figure 2.6 [16]: a comparison of I(Q) and S(Q) calculated from a model of amorphous silicon.

Then Eqn. (2.19) can be written as:

$$\frac{I(Q)}{N} = f(Q)^2 + f(Q)^2 \int_0^{\infty} 4\pi r^2 [\rho(r) - \rho_a] \frac{\sin(Qr)}{Qr} dr. \qquad \textbf{(2.21)}$$

Eqn. (2.21) can be readily inverted using Fourier transform:

$$\Phi(Q) = 4\pi\int_0^{\infty} f(r)\sin(Qr)\,dr,$$

$$f(r) = \frac{1}{2\pi^2}\int_0^{\infty}\Phi(Q)\sin(Qr)\,dQ \qquad \textbf{(2.22)}$$

and the reduced density function $G(r)$ can then be written as:

$$G(r) = 4\pi r[\rho(r) - \rho_a] = \frac{2}{\pi}\int_0^{\infty} Q\frac{\frac{I(Q)}{N} - f(Q)^2}{f(Q)^2}\sin(Qr)\,dQ \qquad \textbf{(2.23)}$$

Rearranging terms in eqn. (2.23), an important equation can be obtained:

$$J(r) = 4\pi r^2\rho(r) = 4\pi r^2\rho_a + \frac{2r}{\pi}\int_0^{\infty} Q\frac{\frac{I(Q)}{N} - f(Q)^2}{f(Q)^2}\sin(Qr)\,dQ \qquad \textbf{(2.24)}$$

which is the radial distribution function (RDF).

The reduced density function $G(r)$ can be obtained from the experimentally measured diffraction intensity and the peaks in $G(r)$ correspond to nearest neighboring distances within the sample. Also the relationship between $G(r)$ and $\rho(r)$ allows $G(r)$ to be integrated to determine coordination numbers

$$C(r_1 - r_2) = \int_{r_1}^{r_2} 4\pi r^2\rho(r)dr = \int_{r_1}^{r_2} r(G(r) - \rho_a)dr \qquad \textbf{(2.25)}$$

where $C(r_1 - r_2)$ is the number of atoms between the radial distances r_1 and r_2 from an atom m.

2.3.4.2 Multiple atomic species

If the sample contains more than one atomic species, it is possible to develop an approximation method of Eqn. (2.15). By introducing a concept called chemically averaged atomic scattering factors [40]. Define U_i as the number of atoms of type i in the specimen, then the chemically averaged atomic scattering factor is:

$$\langle f(Q) \rangle = \frac{1}{N} \sum_{i=1}^{U} U_i f_i(Q) \tag{2.26}$$

and the mean of the square of the chemically averaged atomic scattering factor is:

$$\langle f(Q)^2 \rangle = \frac{1}{N} \sum_{i=1}^{U} U_i {f_i}^2(Q) \tag{2.27}$$

where in both Eqn. (2.26) and Eqn. (2.27) $N = \sum_{i=1}^{U}$.

Furthermore assume that the atomic scattering factor for a particular atomic species is equal to the number of electrons, T_m, of the species multiplied by the chemically averaged atomic scattering factor, which is equivalent to assuming that the atomic scattering factors of the different species are proportional to one another, that is:

$$f_m(Q) = T_m \langle f(q) \rangle. \tag{2.28}$$

Then Eqn. (2.15) becomes:

$$I(Q) = N\langle f(Q)^2 \rangle + \langle f(Q) \rangle^2 \sum_m T_m \sum_{n \neq m} T_n e^{i\mathbf{Q}.\mathbf{r}_{nm}}. \tag{2.29}$$

The second term in Eqn. (2.29) can be split by considering a particular atom m and identifying the different types of neighboring atom i, this gives:

$$I(Q) = N\langle f(Q)^2 \rangle + \langle f(Q) \rangle^2 \sum_m T_m \sum_{i=1}^{V} \sum_{j=1}^{V} T_{ij} e^{i\mathbf{Q}.\mathbf{r}_{(ij)m}} \tag{2.30}$$

where the index pair $(ij) \equiv n \neq m$.

Then introduce $\rho_{mi}(\mathbf{r}_{(ij)m})dV_{(ij)}$ which is the number of atoms of the type i at a distance $\mathbf{r}_{(ij)m}$ from the atom m in a volume element $dV_{(ij)}$, the summation over j can be replaced by an integral over the volume of the sample V [16], then Eqn. (2.30) can be written as:

$$I(Q) = N\langle f(Q)^2\rangle + \langle f(Q)\rangle^2 \sum_m T_m \sum_{i=1}^{U} T_i \int_V \rho_{mi}(\mathbf{r}_{(ij)m}) e^{i\mathbf{Q}\cdot\mathbf{r}_{(ij)m}} dV_{(ij)}. \qquad \textbf{(2.31)}$$

Adding and subtracting of ρ_{a_i}, the density of atoms of type i within the sample, Eqn. (2.31) can be written as:

$$I(Q) = N\langle f(Q)^2\rangle + \langle f(Q)\rangle^2 \sum_m T_m \sum_{i=1}^{U} T_i \int_V [\rho_{mi}(\mathbf{r}_{(ij)m}) - \rho_{a_i}] e^{i\mathbf{Q}\cdot\mathbf{r}_{(ij)m}} dV_{(ij)}. \qquad \textbf{(2.32)}$$

By considering the atom type l in the summation over m and setting $\rho_{li}(\mathbf{r}) = \langle \rho_{mi}(\mathbf{r}_{(ij)m})\rangle_m$, which is the average over all the atoms m of type l, Eqn. (2.32) becomes:

$$I(Q) = N\langle f(Q)^2\rangle + \langle f(Q)\rangle^2 \sum_l U_l T_l \sum_{i=1}^{U} T_i \int_V [\rho_{li}(\mathbf{r}) - \rho_{a_i}] e^{i\mathbf{Q}\cdot\mathbf{r}} dV. \qquad \textbf{(2.33)}$$

Performing the integration in Eqn. (2.33) over the angular components of a spherical coordinate system and noting that $\mathbf{r}$ can be replaced by $r = |\mathbf{r}|$ for an isotropic assembly of atoms gives:

$$I(Q) = N\langle f(Q)^2\rangle + \langle f(Q)\rangle^2 \sum_l U_l T_l \sum_{i=1}^{U} T_i \int_0^{\infty} [\rho_{li}(\mathbf{r}) - \rho_{a_i}] \frac{\sin(Qr)}{Qr} 4\pi r^2 dr. \qquad \textbf{(2.34)}$$

Then by defining:

$$\rho(r) = \frac{1}{N}\sum_{l=1}^{U}\sum_{i=1}^{U} U_l T_l\, T_i \rho_{li}(r) \quad \textbf{(2.35)}$$

and noting:

$$\sum_{l=1}^{U}\sum_{i=1}^{U} U_l T_l\, T_i \rho_{a_i} = N\rho_a \quad \textbf{(2.36)}$$

where ρ_a is the average density of the specimen when all atomic species are included, Eqn. (2.34) can then be written as:

$$I(Q) = N\langle f(Q)^2\rangle + \langle f(Q)\rangle^2 \int_0^\infty [\rho(r) - \rho_a]\frac{\sin(Qr)}{Qr} 4\pi r^2 dr. \quad \textbf{(2.37)}$$

Eqn. (2.37) is analogous to Eqn. (2.22) and can be converted to $G(r)$ in a similar fashion [16].

2.3.4.3 Multiple Elastic Scattering

In previous process the single scattering assumption or the so-called kinematical approximation was applied in Eqn. (2.10) which was equivalent to assume that the amplitude of scattered electrons was very small when compared with the amplitude of the incident electrons. The assumption of single scattering is based on the relationship between Z, the thickness of the specimen, and λ_e the mean free path for elastic scattering (i.e. the average distance that an electron travels between two elastic scattering events) [14]. So the probability of multiple scattering increases as the ratio $\frac{Z}{\lambda_e}$ increases.

Anstis et al. [41] has developed a theoretical treatment of the multiple elastic scattering in amorphous materials and proved that it is possible to recover the single scattering intensity distribution from the multiply scattered intensity distribution using Fourier-log deconvolution techniques because of the independent nature of multiple scattering in amorphous materials. Thus it is possible to perform $G(r)$ analysis on specimens too thick to satisfy the kinematical approximation [16].

2.3.5 Conclusion of Electron Diffraction of Amorphous Materials

Electrons are elastically scattered from atomic potentials and form a diffraction pattern which is experimentally measurable. The data is then transformed to obtain structural information about the sample. It has been shown that it is possible to obtain structural information from a sample. For example, D. Cockayne and his colleagues [26] reported that the nearest-neighbour distances together with coordination numbers can be obtained from small chosen regions of specimens by using the reduced density function technique.

2.4 Thickness Measurement of TEM Specimens

2.4.1 Introduction to Thickness Measurement

In TEM studies the specimen thickness is of importance. With knowing the thickness it is possible to calculate the structure factors, cross-sections or mean free paths for elastic or inelastic scattering, and it is also possible to determine the concentration of defects and precipitates from micrographs. Furthermore, the to explore the effect on the electron diffraction in TEM of thickness, it is also necessary to measure the specimen thickness.

Currently there are a variety of methods available to determine the thickness of the TEM specimen all depending on one or more of the principles include: parallax measurements of known features at two or more angles; measure the X-ray intensity (continuum or characteristic) or electron energy loss s spectroscopy (EELS) signal in known experimental conditions; fine detail produced by diffraction in the images or diffraction patterns of crystalline specimens [42].

For the diffraction-based techniques, they can give an accuracy of 5% or even more and usually are considered as the most accurate method. However, it is time-consuming and the disadvantage also includes that they can only be applied to single-crystal specimens or crystalline regions. Meanwhile, skills are required to interpret the experimental data as well as to precisely orient specimen.

Methods based on calibrating the intensity of X-ray emission from specimens are in principle tedious to establish but very rapid to use once the calibration has been done [42], this method is capable of giving the mass-thickness. However, their applications need the experimental conditions to be precisely reproducible and mass loss may also be a problem because the measurement involves a substantial electron dose to the specimen. EELS method is another method requires no knowledge of the physical or chemical properties of the specimen other than its refractive index [43]. Both the X-ray intensity method and the EELS method can be used to determine the thickness of an amorphous sample or a polycrystalline one that is far from any strong diffracting orientation and the CBED method cannot be used.

Methods based on parallax measurements are widely used. To record two images under similar conditions, at two different but known specimen tilts, as long as some features can be recognised on both surfaces, the thickness can then be calculated. For example, the contamination spots separation (CSS) method. The advantage of this method is that it is extremely simple to use, the interpretation skills required are negligible; it gives the thickness at the point where you want it; and it’s also can be applied to amorphous or polycrystalline samples.

In the following section, CBED method, EELS method, CSS method and EDX method will be discussed in more detail.

2.4.2 CBED Method

A useful application of CBED patterns is to measure the thickness of a crystal. This method can be applied at a two-beam condition either under strong (Kelly et al., 1975) or under weak beam conditions (Botros, 1995). TEM imaging at a two-beam condition can also give an estimate of linear thickness through the extinction contours (Hirsch et al., 1965) [44]. The advantage of this method is that the foil thickness can be measured at precisely the point where diffraction and microanalysis are taken. The method is, of course, limited to crystalline specimens, but it is one of the most popular and accurate method of thickness determination of fully crystalline materials [23].

Basically this method is based on the variation of the intensity of the diffracted beam with thickness known as Pendellösung Fringes [45]. A convergent beam is used to limit the region of specimen that contributes to the diffraction pattern. In addition to the improved spatial resolution, CBED yields information not available in selected area diffraction (SAD) patterns. When exactly in a zone-axis, the 000 disc usually contains concentric diffuse fringes known as Kossel-Möllenstedt (K-M) fringes. The number of these fringes increases with one every time when the thickness increases by one extinction distance, ξ_g. If the specimen is less than one extinction distance, then no fringes will appear and the 000 disc is uniformly bright. To get the most out of a CBED pattern, the specimen should be thicker than one extinction distance. The region of the foil selected should be relatively flat and undistorted, and the beam must be focused at the plane of the specimen.

However, in practice the thickness measurements are not made under zone-axis conditions but under two-beam conditions with only one strongly excited *hkl* reflection. The CBED discs will then contain parallel instead of concentric intensity oscillations. These oscillations are symmetric in the *hkl* disk and asymmetric in the 000 disk. Actually these fringes are equivalent to the rocking-curve intensity oscillations which occur across a bend contour in a bright field image. The central bright fringe is in the exact Bragg condition where $\mathbf{s} = 0$. The fringe spacings correspond to angles $\Delta\theta_i$ and from this spacing the deviation s_i for the ith fringe can be determined according to:

$$s_i = \lambda \frac{\Delta\theta_i}{2\theta_B d^2} \quad \textbf{(2.38)}$$

where λ is the wavelength of the incoming electrons, θ_B is the Bragg angle for the diffracting *hkl* plane and d is the *hkl* interplanar spacing. s_i can be measured directly from the spacing of the fringes in the convergent beam pattern and $\Delta\theta_i$ is the distance to the chosen minimum from the mid-line and the angle $2\theta_B$ is the separation of the 000 and *hkl* disks.

If the extinction distance ξ_g is known, then the foil thickness t can be determined according to:

$$\frac{s_i^2}{n_k^2} + \frac{1}{\xi_g^2 n_k^2} = \frac{1}{t^2} \quad \textbf{(2.39)}$$

where n_k is an integer.

If the extinction distance ξ_g is unknown, a graphical method can be used, plotting the measurements for several fringes. These integers will be assigned to the fringes, starting with n=1 for the first fringe, then assign n=2 to the second fringe, etc. Then plotting $(s_i/n_k)^2$ versus $(1/n_k)^2$, if the results is a straight line, the thickness t is given by the intercept of the resulting straight line with the $(s_i/n_k)^2$ axis (as shown in figure 2.8). When this is not possible, n=2 should be assigned to the first fringe. Continue to iterate until a straight line is achieved.

Usually the accuracy of the two-beam methods depends on how well the two-beam condition is approximated during the experiment. A more accurate technique is based on comparing measured, energy-filtered CBED patterns with calculated ones, where the comparison is carried out as a fitting of structure factors and thicknesses to minimize the difference between the calculated and measured patterns (Zuo and Spence 1993; Bird and Saunders, 1992; Saunders et al., 1996; Rossouw et al., 1996; Deininger et al., 1994).

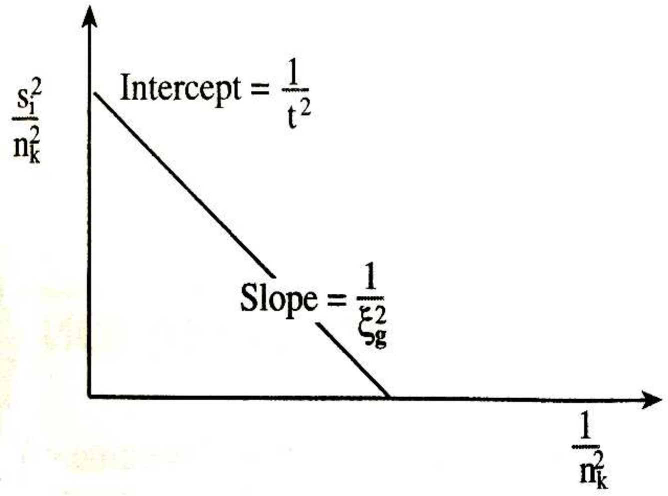

Figure 2.7: plot the $(s_i/n_k)^2$ *vs.* $(1/n_k)^2$*, if the plot is a straight line, extrapolate to the ordinate to find t.*

2.4.3 EELS Method

Electron energy-loss spectroscopy (EELS) is an analytical technique that measures the change in kinetic energy of electrons after they have interacted with a specimen [46]. When carried out in a modern TEM, EELS is capable of giving structural and chemical information about a solid, with a spatial resolution down to the atomic level in favorable cases. Compare with other methods for specimen thickness measurement, EELS is more general (applicable to crystalline and amorphous samples) and relatively rapid (it involves recording the low-loss spectrum, where the intensity is relatively high).

There are different ways of using EELS to measure the thickness, the most common procedure is the log-ratio method that is based on the measurement of the integrated intensity I_0 of a zero-loss peak relative to the integral intensity I_t of the whole spectrum [46].

Poisson statistics of inelastic scattering:

$$P_n = (1/n_!)(t/L)^n \exp(-t/L) \qquad .(\mathbf{2.40})$$

lead to the formula [46]:

$$t/L = \log_e(I_t/I_0) \qquad (\mathbf{2.41})$$

where L is a plasmon or total-inelastic MFP. To capture most of the intensity, I_t needs only be integrated up to about 200 eV, assuming a typically thin TEM specimen (such as $t < 200$ nm). If necessary, the spectrum can be extrapolated until the spectral intensity becomes negligible. The ratio t/L provides a measure of the relative thickness of different areas of a specimen (if it has a uniform composition); knowing the absolute thickness t requires a value of the inelastic MFP for the incident-electron energy E_0 and collection angle β used to record the data. If no angle-limiting TEM aperture is used, lens bores limit β to a value in the range 100–200 mrad, large enough to make L a total MFP, which is tabulated for common materials at electron energies of 100 and 200 keV (Egerton, 1996; Iakoubovskii et al, 2008). This MFP is also appropriate when a large TEM objective aperture is used, although a correction for incident-probe convergence (semi-angle α) may then be necessary (Iakoubovskii et al, 2008).

If the collection angle β is small enough, a β-dependent MFP can be estimated from [46]:

$$L_p(\beta) \approx (4a_0\, T/E_p)\left[\ln\left(1 + \beta^2/\theta_{Ep}^2\right)\right]^{-1} \qquad \textbf{(2.42)}$$

with E_p taken as the energy of the main peak in the low-loss spectrum. If the mean atomic number of the specimen is known, other empirical procedures are available for calculating L (E_0, β) (Egerton 1996). The accuracy of the log-ratio method depends largely on how well the MFP is known, which varies from one material to another, but as a rough guide, thickness can probably be measured to about 20% accuracy in most cases [46].

2.4.4 CSS Method

The irradiation of a small electron beam on a specimen results in a pair of contamination deposits both on the top and bottom surfaces of the specimen. The parallax of these two deposits after tilting the specimen can be used to calculate the specimen thickness. Knowing the angle of the sample tilted and the distance between two deposits, it’s easy to mathematically calculate the specimen thickness. This method is applicable to different materials and has been favored especially for specimens that have been highly irradiated in a nuclear reactor since no thickness fringes appear owing to the high density of radiation-introduced defects [47].

2.4.5 EDX Method

This method is carried out using a TEM by utilising the relationship between the foil thickness and the gross integral of the characteristic energy dispersive x-ray (EDX) spectrum.

There is a reproducible linear relationship between the characteristic X-ray intensity of a specific element (i.e. element A) and the specimen thickness for TEM thin film, it is because in TEM thin films, electrons lose only a small fraction of their energy in the film (~5 eV/nm), in addition, few electrons are backscattered and the trajectory of the electrons in the sample can be assumed to be the same as the thickness of the specimen film [24]. Under these circumstances, the generated characteristic X-ray intensity of element A, $\mathrm{I_A^*}$ can be given by a simplified formula:

$$\mathrm{I_A^*} = \frac{\mathrm{KC_A Q_A \omega_A a_A}}{\mathrm{A_A}}\mathrm{t}. \qquad \textbf{(2.43)}$$

where K is a material-dependent constant with units ($\mathrm{g/cm^3}$)(atoms/mol), $\mathrm{C_A}$ is the weight fraction of element A (dimensionless), $\mathrm{Q_A}$ is the ionization cross section ($\mathrm{cm^2/atom}$), ω_A is the fluorescence yield (ionization fraction resulting in X-ray emission) (dimensionless), $\mathrm{a_A}$ is the relative intensity factor (fraction of the total measured K line intensity of element A) (dimensionless), $\mathrm{A_A}$ is the atomic weight of element A ($\mathrm{g/mol}$) and t is the thickness of the element A specimen film (membrane) (cm) [24].

Once the relationship between element A X-ray intensity and the TEM specimen thickness is formed, it is possible to calculate the thickness of the TEM specimen in a certain microscope condition by calculating each item in Eqn. (2.43).

References

[1] IAEA, *The Principles of Radioactive Waste Managemen*t, 1995.

[2] IAEA, *Classification of Radioactive Waste, A Safety Guide*, 1994.

[3] IAEA, *Strategy and Methodology for Radioactive Waste Characterization*, 2007.

[4] M. I. Ojovan, W. E. Lee, *An Introduction to Nuclear Waste Immobilisation*, Elsevier, 2005, p. 315.

[5] NRC, *Nuclear Wastes: Technologies for Separation and Transmutation*, National Academy Press, 1996.

[6] W. R. Wilmarth, J. T. Mills, V. H. Dukes, J. Separation Sci. Tech. 40 (2005) 255-265.

[7] E. Gomez, D. Amutha Rani, C. R. Cheeseman, D. Deegan, M. Wise, A. R. Boccaccini, J. Hazard. Mater. 161 (2009) 614-626.

[8] D. Deegan, C. Scales, Proc. 11th Int. Conference on Environmental Remediation

and Radioactive Waste Management (2007) ICEM07-7271.

[9] Tetronics Ltd, *The Role of Tetronics Plasma Vitrification Technology in Nuclear Waste Management*, 2006.

[10] K. Moustakas, D. Fatta, S. Malamis, K. Haralambous, M. Loizidou, J. Hazard. Mater. B123 (2005) 120-126.

[11] J. A. Roether, D. J. Daniel, D. Amutha Rani, D. E. Deegan, C. R. Cheeseman, A. R. Boccaccini, J. Hazard. Mater. 173 (2010) 563-569.

[12] C. P. Yoganand, V. Selvarajan, L. Lusvarghi, Curr. Appl. Phys. 9 (2009) 839-846.

[13] Aurora López-Delgado, Hanan Tayibi, Carlos Pérez, Francisco José Alguacil, Félix Antonio López, J. Hazard. Mater. 165 (2009) 180-186.

[14] D. B. Williams, C. B. Carter, *Transmission Electron Microscopy: A Textbook for Materials Science*, Plenum Press, 1996.

[15] H. Hirai, Y. Tabira, K. Kondo, T. Oikawa, N. Ishizawa, Phys. Rev. B 52 (1995) 6162.

[16] W. E. McBride, PhD Thesis, University of Sydney, 1999.

[17] D. A. McQuarrie, *Statistical Mechanics*, Harper & Row, 1976, p. 257-260.

[18] A. Howie, O. L. Krivanek, M. L. Rudee, Phil. Mag. 27 (1973) 235-255.

[19] M. L. Rudee, A. Howie, Phil. Mag. 25 (1972) 1001-1007.

[20] J. M. Gibson, M. M. J. Treacy, Phys. Rev. Lett. 78 (1997) 1074-1077.

[21] A. Howie, C. A. McGill, J. M. Rodenburg, J. Phys. Colloque 46 C9 (1985) 59-62.

[22] J. M. Rodenburg, J. Phys. Colloque 46 C9 (1985) 63-68.

[23] D. B. Williams, *Practical Analytical Electron Microscopy in Materials Science*, Verlag Chemie International, 1984.

[24] D. C. Joy, A. D. Romig Jr., J. I. Goldstein, (Ed.), *Principals of Analytical Electron Microscopy*, Plenum Press, 1986.

[25] M. M. Disko, C. C. Ahn, *Transmission Electron Energy Loss Spectrometry in Materials Science*, A Publication of TMS Minerals, Metals, Materials, 1990.

[26] D. J. H. Cockayne, D. R. McKenzie, Acta Cryst. (1988) A44 870-878.

[27] O. L. Krivanek, C. C. Ahn, R. B. Keeney, Ultramicroscopy 22 (1987) 103-116.

[28]L. Pauling, L. O. Brockway, J. Am. Chem. Soc. 57 (1935) 2684-2692.

[29]D. Halliday, R. Rensnick, *Fundamentals of Physics*, John Wiley & Sons, 1988, p. 209.

[30]L. de Broglie, Ann. de Phys. 3 (1925) 22.

[31]J. Mehra, H. Rechenberg, *The Historical Development of Quantum Theory*, Springer-Verlag, 1982.

[32]R. Shankar, *Principles of Quantum Mechanics*, Kluwer Academic/Plenum Publishers, 1994, p. 143-145.

[33]J. D. Jackson, *Classic Electrodynamics*, Wiley, 1998.

[34]L. M. Peng, S. L. Dudarew, M. J. Whelan, *High-Energy Electron Diffraction and Microscopy*, Oxford Science Publications, 2004.

[35]J. J. Sakurai, *Modern Quantum Mechanics*, Addison Wesley, 1994.

[36]R. N. Bracewell, *The Fourier Transform and Its Applications*, Boston: McGraw Hill, 2000.

[37]D. McKie, C. McKie, *Essentials of Crystallography*, Blackwell Scientific Publications, 1992.

[38]J. M. Cowley, *Diffraction Physics*, North-Holland Physics Publishing, 1981.

[39]M. Lake, PhD Thesis, University of Sydney, 1988.

[40]D. C. Green, PhD Thesis, University of Sydney, 1991.

[41]G. R. Anstis, Z. Liu, M. Lake, Ultramicroscopy 26 (1988) 65-70.

[42]P. J. Goodhew, D. Chescoe, Micron. 11 (1980) 153-181.

[43]R. F. Egerton, S. C. Cheng, Ultramicroscopy 21 (1987) 231-244.

[44]J. L. Labar, J. Morgiel, Micron. 29 (1998) 425-430.

[45]P. M. Kelly, A. Josntons, R. G. Blake, J. G. Napier, J. Appl. Phys. 62 (1975) 419.

[46]R. F. Egerton, Rep. Prog. Phys. 72 (2009) 016502.

[47]T. Sawai, M. Suzuki, Scripta Metallurgica 24 (1990) 2047-2052.

CHAPTER THREE

EXPERIMENTAL PROCEDURES

Two samples were provided by the Tetronics Ltd and used in this project. For microstructure characterisation, X-ray diffractometry (XRD), scanning electron microscopy (SEM) and transmission electron microscopy (TEM) were carried out. The mechanical properties of the two samples were studied using Vickers hardness test and compression test. The chemical stability was characterised by measuring the dissolution rate of the samples in alkaline solution.

3.1 Microstructure Characterisation

3.1.1 X-ray Diffractometry (XRD)

Samples for XRD were cut into dimensions of 5 mm×10 mm×20 mm. Sample surface was ground using 1200-grit Si-C papers and polished to a mirror-like finish. XRD experiments were performed at room temperature on a Hiltonbrooks-1158 X-ray diffractometer using Cu Kα (λ=1.5418 Å) radiation. 2θ scan was performed over a range from 15° to 100° with a step size of 0.02° at 2 seconds per step.

3.1.2 Scanning Electron Microscopy (SEM)

SEM was used to study the microstructure and to obtain the chemical information from the samples. Samples for SEM studies were mounted in epoxy resin and then progressively ground using SiC papers and finally polished to a mirror like finish with Au coaching. A Philips XL-30 SEM and a JEOL-7000 SEM equipped with energy dispersive X-ray spectrometer (EDX) were used to study the morphology and chemical composition of the samples.

Backscattered electron (BSE) mode was used in SEM study. In BSE, the backscattered electrons are the electrons resulting from the collision between the electron beam and atoms deep within the specimen (shown in Figure 3.1 [1]). The fraction of the incident beam backscattered depends on the mass density, or more accurately, the average atomic number of the specimen. So the backscattered electron signal is able to resolve local variations in mass density and results in atomic number contrast. The element of higher atomic number can show stronger emission and brighter areas on the screen.

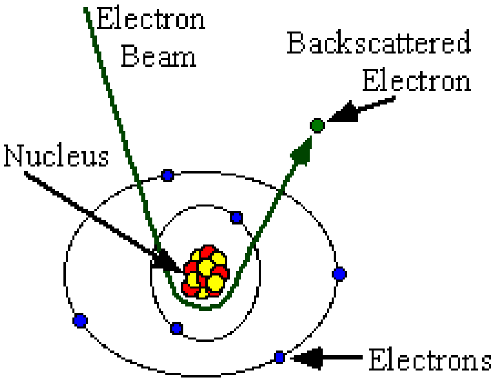

Figure 3.1: interaction between electron beam and specimen producing backscattered electrons [1].

3.1.3 Transmission Electron Microscopy (TEM)

Samples for TEM observation were prepared using a focused ion beam (FIB) microscope. Sample A has two different areas named the green area (Sample A-Green) and the white area (Sample A-White) while Sample B shows green colour only. A pure aluminum foil sample prepared by twin-jet polishing was used to characterise and confirm the relationship between the specimen thickness and the X-ray intensity collected under prescribed conditions and the results were used as a reference for the determination of the effects of specimen thickness on the electron diffraction in the current study.

Both JEM-2100 and TECHNAI F20 microscopes (shown in Figure 3.2) were used to study the microstructure of the samples at 200 kV. TEM images were taken to study the morphology and the selected area electron diffraction (SAD) was carried out to derive the structural information while EDX measurement was also performed at same areas. For the aluminum reference sample, convergent beam electron diffraction

(CBED) was used to measure the thickness of the specimen and EDX was performed at the sample positions.

Electron diffraction patterns obtained from Samples A and B were transformed into the reduced density function (RDF) mathematically and the microstructural information was obtained.

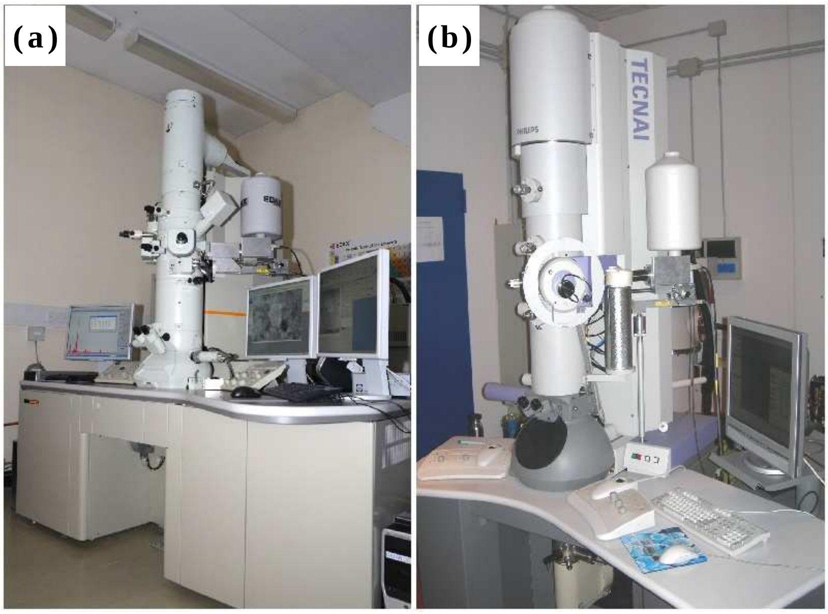

Figure 3.2: images showing a JEM-2100 TEM (a) and a TECHNAI F20 TEM (b).

3.2 Mechanical Properties

3.2.1 Compression Test

Compression tests were performed using a Zwick-1484 machine with a 200 kN load cell as shown in Figure 3.3. Samples with dimensions of about 5 mm×5 mm×10 mm were cut out and then polished to a mirror like finish. The strain rate was set at 0.05 min^{-1}.

Figure 3.3: image showing the ZWICIK-1484 mechanical test machine used in the study.

3.2.2 Vickers Hardness

In order to measure the micro-hardness, Samples were mounted and then mechanically polished down to a mirror like finish. A Vickers micro-hardness tester was used with a 200 gram load and 10 seconds holding time. The micro-hardness tests were repeated and an average of 6 measurements was recorded.

3.3 Chemical Stability

3.3.1 Dissolution in Alkaline Solution

Alkaline solutions were prepared by dissolving analytical reagent-grade [NaOH] in distilled water. The concentrations of [NaOH] in the solution were set at 0.1 mol/dm^3, 0.2 mol/dm^3, 0.5 mol/dm^3 and 1.0 mol/dm^3, respectively. Samples were firstly cut into dimensions of 5 mm×5 mm×10 mm and then immersed in the alkaline solution for various periods of time. During this process the samples were periodically taken out to measure the weight loss. In the first two days the samples were measured every four hours and then every twelve hours for the following twelve days.

References

[1] http://mse.iastate.edu/microscopy/backscat2.html, Iowa State University.

CHAPTER FOUR

RESULTS AND DISCUSSION

The characterisation results of the samples are presented in two sections. Section 4.1 contains the microstructural information analysis given by XRD, SEM and TEM, respectively. The chemical composition of the samples is also presented in this section. Section 4.2 shows the results of mechanical properties test including Vickers hardness and compressive strength, the chemical stability analysis of the samples in alkaline solution is also given in this section.

There are two different types of samples named Sample A and Sample B. Sample A is sodium-free and contains more MgO and Al_2O_3. Sample B is sodium-contained and contains more SiO_2. The optical images of Sample A and Sample B are shown in Figure 4.1. Sample A is mainly in green colour with small areas in white while Sample B is completely in green. In the following chapters the green area of Sample A is named Sample A-Green and the white area of Sample A is named Sample A-White.

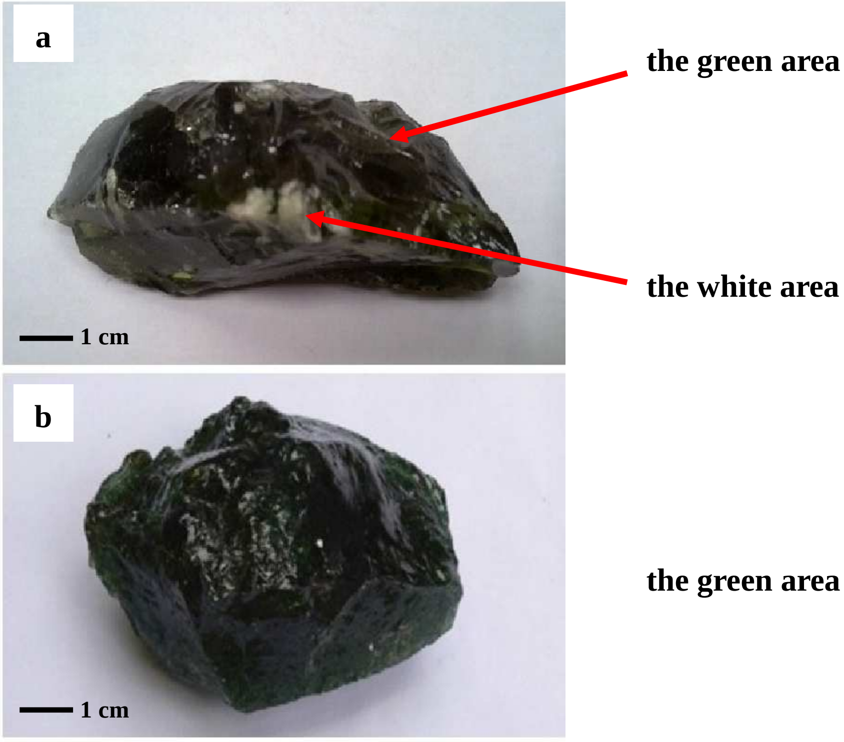

Figure 4.1: optical images showing (a) Sample A which has two different areas: the green area and the white area and (b) Sample B in green.

4.1 Microstructure Characterisation

4.1.1 X-ray Diffractometry (XRD)

XRD was performed using a Hiltonbrooks-1158 X-ray diffractometer at room temperature using Cu Kα radiation. Only Sample A-Green and Sample B were selected to perform XRD, because from the optical images it is easy to find that Sample A-Green is the main part of Sample A and Sample A-White only accounts for a small fraction. For a more accurate characterisation, Sample A-White was characterised using TEM separately and the results will be discussed in later sections.

Several samples for XRD were extracted and prepared from Sample A-Green and Sample B, respectively. 2θ scan was performed from 15° to 100° and the step size and step time were adjusted to 0.02° and 2 seconds per step. The XRD analysis was repeated for several times on these samples and the results showed good consistency, so two typical XRD patterns obtained from Sample A-Green and Sample B are demonstrated in Figure 4.2 and Figure 4.3, respectively.

For crystalline materials, the atoms are arranged regularly which gives sharp and narrow diffraction peaks in XRD patterns. However, in amorphous materials atoms are arranged in a random way similar to which in a liquid and gives a very broad peak (halo). Figure 4.2 shows the typical XRD pattern obtained from Sample A-Green. The featureless diffractogram indicates that this optically green sample is completely amorphous and no crystalline phase is observed. Figure 4.3 shows the typical XRD pattern obtained from Sample B also indicating the amorphous nature of Sample B. A broad peak at $2\theta \sim 24^{\circ}$ can be found at Figure 4.2, a similar peak can be observed at Figure 4.3 but not as clear as at Figure 4.3. It has been reported that the diffused broad peak at around $2\theta \sim 24^{\circ}$ may be associated with that usually observed in amorphous silicates [1, 2].

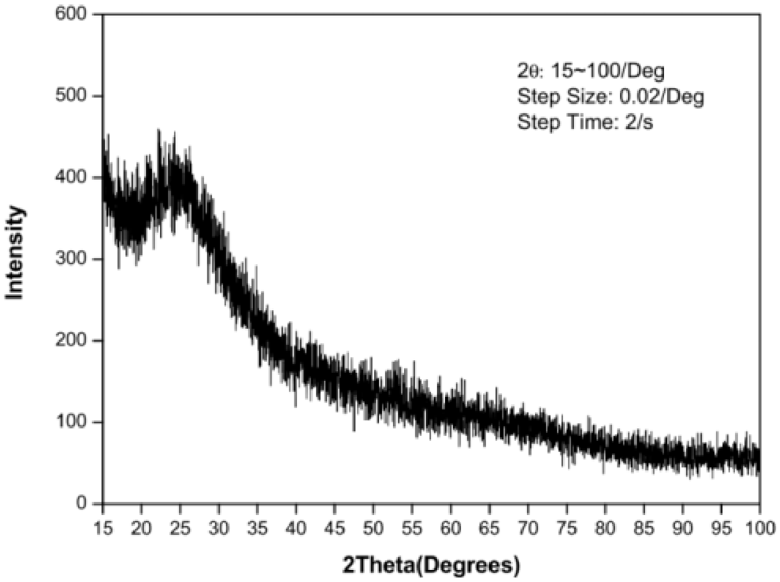

Figure 4.2: a typical XRD pattern obtained from Sample A-Green.

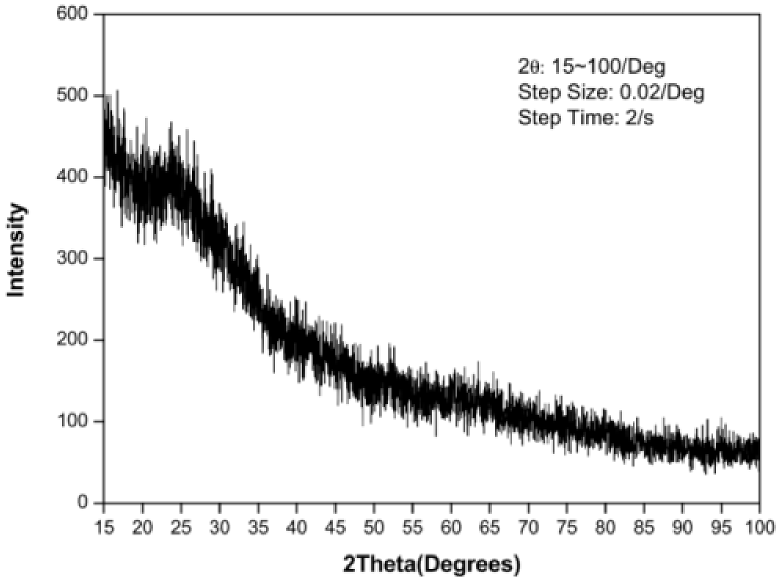

Figure 4.3: a typical XRD pattern obtained from Sample B.

4.1.2 Scanning Electron Microscopy (SEM)

SEM was used to study the microstructure and chemical composition of the samples. The polished samples were gold coated before SEM observations.

4.2.1.1 Different Regions in Sample A

Figure 4.4 shows the SEM micrographs in backscattered electron (BSE) mode obtained from Sample A-Green and Sample A-White, respectively. From Figure 4.4 (a) it can be found that the green area in Sample A has a homogeneous microstructure. However, Figure 4.4 (b) which obtained from the white area in Sample A indicates a dendrite-like structure that contains grey parts and bright parts.

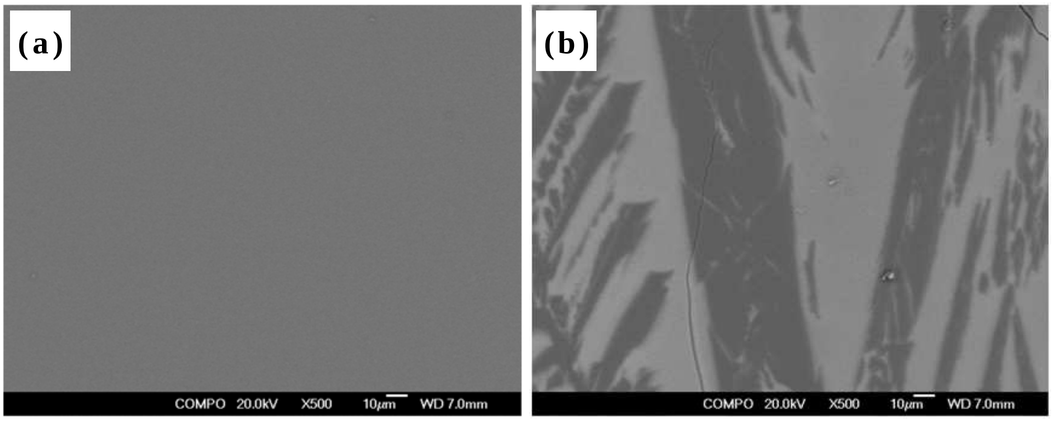

Figure 4.4: SEM micrographs in backscattered electron (BSE) mode showing Sample A-Green (a) and Sample A-White (b).

The contrast from features visible in BSE images may arise from three factors. First is the atomic number contrast because the signals backscattered increase with increasing average atomic number of the specimen, it reflects variations in specimen mass density that associated with variations in composition [3]; second is specimen topography because when tilt the specimen surface towards a backscattered electron detector can give an enhanced signal while the signal is reduced if the surface is tilted away from the detector; third is the crystallography of the specimen, the crystallographic orientation and defects may produce the contrast in BSE images via channeling effect [4]. The grey region and the bright region in Figure 4.4 (b) may be related to the average atomic number of each region because in amorphous materials no strains and crystallographic orientation exist.

Table 4.2: the summary of EDX results showing the chemical compositions in atomic percentage obtained from Sample A-Green and the grey region and the bright region in Sample A-White respectively.

Sample A-Green	**at.%**		**at.%**
O	63% ± 0.2	**Ce**	0.7% ± 0.1
Mg	9% ± 0.2	**Ti**	0.3% ± 0.1
Al	7% ± 0.2		
Si	20% ± 0.3		
Sample A-White (grey region)	**at.%**		**at.%**
O	62% ± 0.1	**Ce**	0.4% ± 0.1
Mg	13% ± 0.3	**Ti**	0.2% ± 0.1
Al	5% ± 0.2		
Si	19% ± 0.1		
Sample A-White (bright region)	**at.%**		**at.%**
O	63% ± 0.3	**Ce**	1.2% ± 0.1
Mg	6% ± 0.4	**Ti**	0.4% ± 0.1
Al	9% ± 0.3		
Si	21% ± 0.3		

Table 4.2 is the summary of EDX results showing the chemical compositions in atomic percentage obtained from Sample A-Green and the grey region and bright region in Sample A-White respectively. For Sample A-Green, O, Mg, Al, and Si with atomic percentage of 63%, 9%, 7% and 20% are mentioned, small amount of Ce, Ti, also exist in Sample A-Green. The grey region in Sample A-White also contains O, Mg, Al, and Si of 62 at.%, 13 at.%, 5 at.% and 19 at.%, Ce and Ti are also observed in Sample A-White. The bright region in Sample A-White also contains O, Mg, Al, and Si of 63 at.%, 6 at.%, 9 at.% and 21 at.% and small amount of Ce and Ti as well. In addition, very small fraction of Fe and Ca can be detected in all the three regions. There trace elements may be introduced artificially. Compare with the grey region in Sample A-White, the bright region in Sample A-White contains more Al (9 at.%), Si (21 at.%), Ce (1.2 at.%) and less Mg (6 at.%). The difference of chemical composition between the grey region and the bright region in Sample A-White may arise the contrast shown in Figure 4.4 (b).

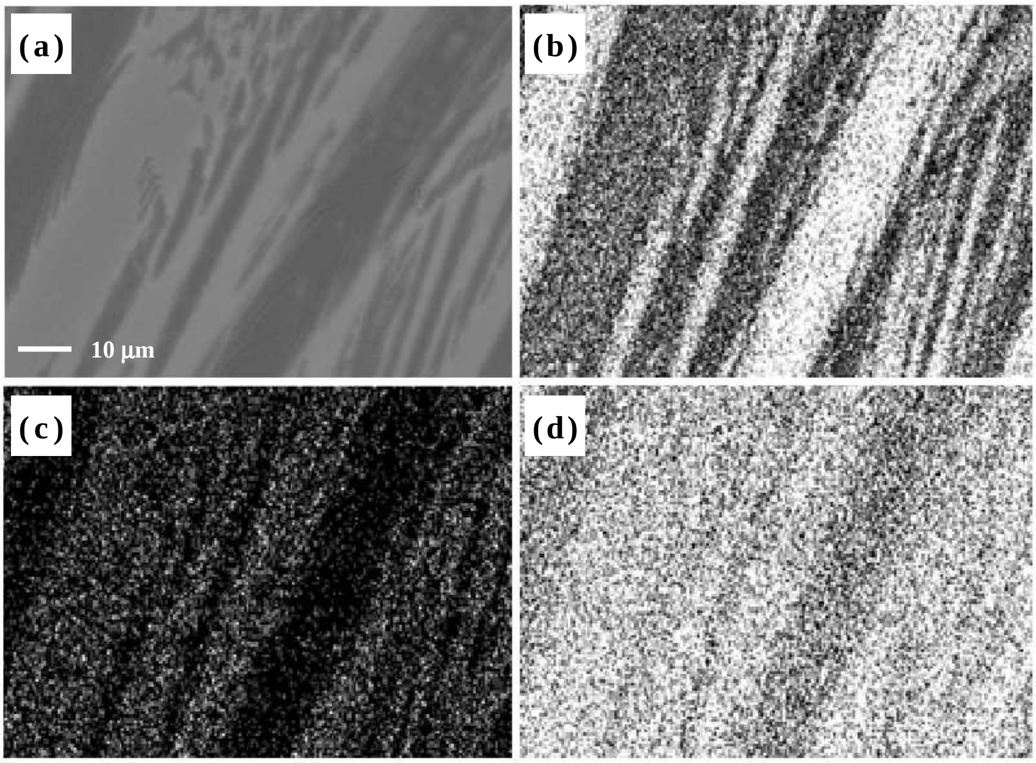

Figure 4.5: elemental mapping results of (a) an area contains the typical dendrite-like structure in Sample; (b) is the Mg map, (c) is the Al map and (d) is the Ce map.

The previous EDX results of Sample A-White were obtained from a series of spots of the specimen. Furthermore, to confirm the obtained EDX results, elemental mapping was performed in a typical white area in Sample A which showed a dendrite-like two-phase structure. It can be found that the bright region contains less Mg (Figure 4.5 (b)) and more Al, Ce (Figure 4.5 (c) and (d)). This shows good consistency with the previous EDX results.

4.2.1.2 Comparison between Sample A and Sample B

Figure 4.6 shows the SEM micrographs in backscattered electron (BSE) mode of the green area of Sample A and Sample B, respectively. Compare with the homogeneous microstructure of the green area of Sample A (Figure 4.6 (a)), Sample B (Figure 4.6 (b)) contains some black fiber-like structure.

Table 4.3 is the summary of EDX results showing the chemical compositions in atomic percentage obtained from the green area of Sample A and Sample B. The EDX results of Sample B were obtained from matrix area (not the black fibers). Compare with the green area of Sample A, Sample B contains O, Mg, Al, Si and Na of 65 at.%, 3 at.%, 5 at.%, 22 at.% and 4 at.%. A new element Na is observed as a new major element. In addition, very small fraction of K and Fe were detected in Sample B.

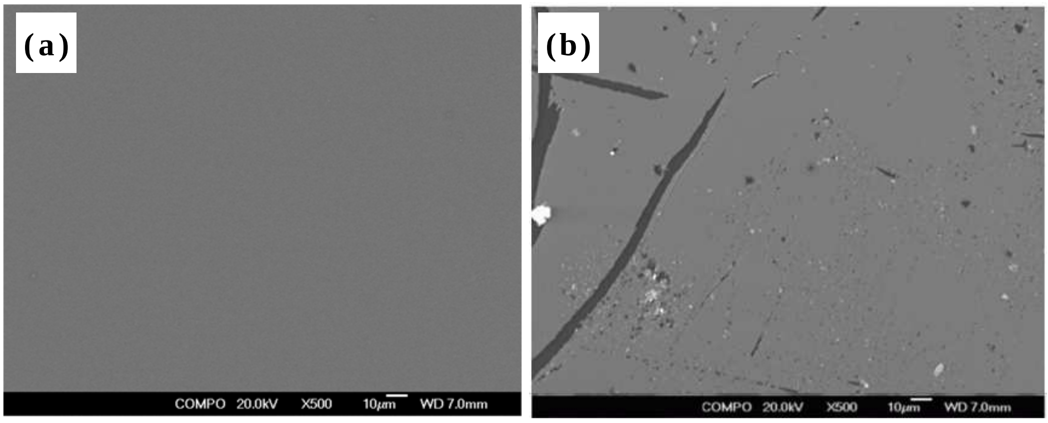

Figure 4.6: SEM micrographs in backscattered electron (BSE) mode showing Sample A-Green (a) and Sample B (b).

Table 4.3: the summary of EDX results showing the chemical compositions in atomic percentage obtained from the green area of Sample A and Sample B.

Sample A-Green	**at.%**		**at.%**
O	63% ± 0.2	**Ce**	0.7% ± 0.1
Mg	9% ± 0.2	**Ti**	0.3% ± 0.1
Al	7% ± 0.2		
Si	20% ± 0.3		
Sample B	**at.%**		**at.%**
O	65% ± 0.8	**K**	0.3% ± 0.1
Mg	3% ± 0.1	**Fe**	0.4% ± 0.1
Al	5% ± 0.1		
Si	22% ± 0.6		
Na	4% ± 0.2		

A further study on the black fiber-like structure observed in Sample B was carried out. Figure 4.7 (a) is the bright field (BF) TEM image showing the black fiber-like structure exists in Sample B and (b) is the electron diffraction pattern taken from the black fiber and indicates that it is amorphous. A line scan was performed to study the chemical composition of the black fiber-like structure. Figure 4.8 shows where the line scan was performed and Figure 4.9 shows the line scan results of the black fiber-like structure. The line scan was performed from point A to point B with a distance of about 300 nm, and line scan profile was obtained using the concentration of each element versus the distance. Figure 4.10 (a) is the profile with the concentration scale 0-80 (at.%), at this higher concentration profile more O and lower Si were observed. Figure 4.10 (b) with lower concentration scale 0-5 (at.%) shows that in this profile Ga, Mg and Al have higher concentrations in the fiber-like structure. Ga was probably introduced form the FIB process.

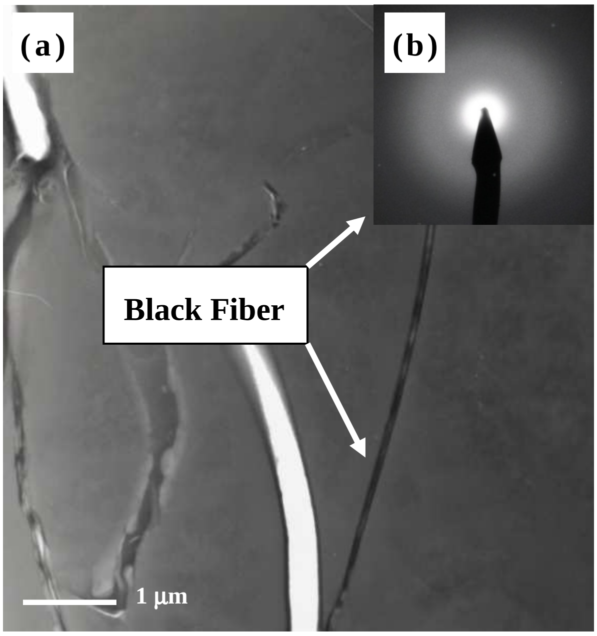

Figure 4.7: (a) TEM image of Sample B showing the existence of the black fiber-like structure and (b) SAD pattern performed at the black fiber-like structure showing an amorphous structure.

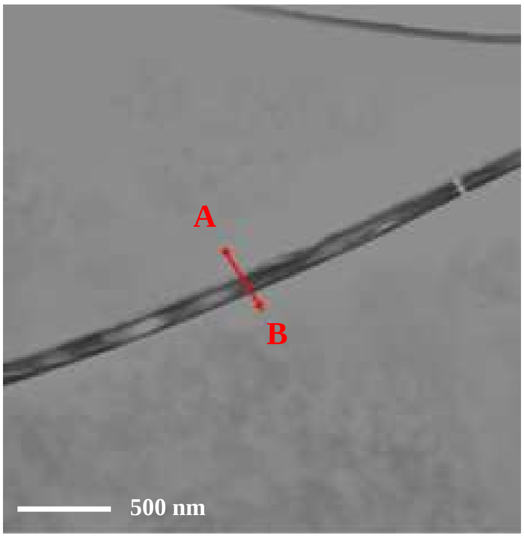

Figure 4.8: bright field TEM image showing where the line scan was performed.

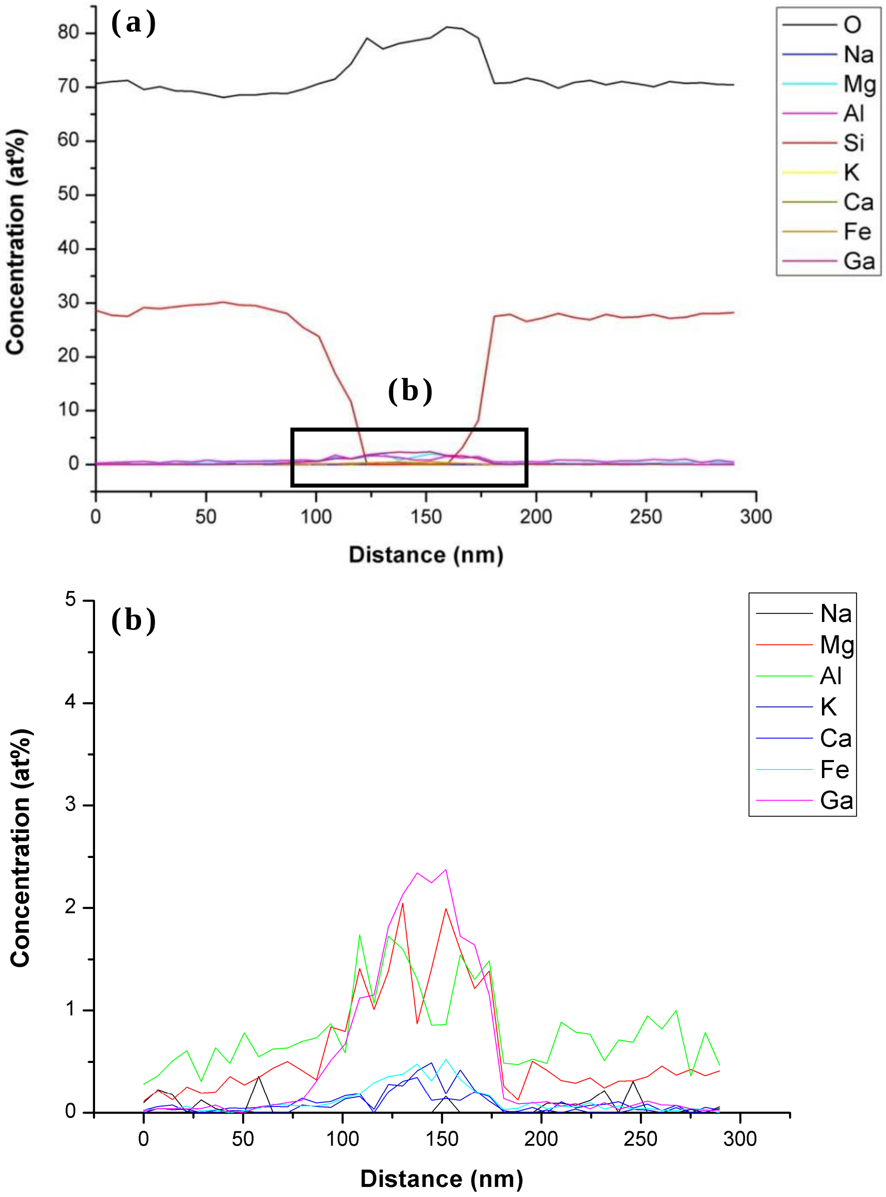

Figure 4.9: line scan profiles performed through the black fiber-like structure: (a) is the profile with concentration scale 0 to 80 (at.%) and (b) is the same profile with concentration scale 0 to 5 (at.%).

4.1.3 Transmission Electron Microscopy (TEM)

TEM was used to study the microstructure of the samples. TEM specimens were prepared by FIB microscope, another pure aluminum foil sample was prepared by twin-jet polishing for reference. Thickness measurement of TEM specimens and electron diffraction study of the samples are also presented in this section.

Figure 4.10 (a) FIB image shows the position where this image was taken from, (b) shows its electron diffraction pattern and (c) shows the TEM image obtained from Sample A-Green. The electron diffraction pattern of Sample A-Green indicates an amorphous structure because a diffuse ring typical for amorphous material is observed. This is confirmed by the TEM image which also shows an amorphous nature.

Figure 4.11 (a) FIB image shows the position where this image was taken from, (b) shows its electron diffraction pattern and (c) shows the TEM image obtained from Sample A-White. The electron diffraction pattern of Sample A-White also indicates an amorphous structure which is confirmed by its TEM image.

Figure 4.12 (a) FIB image shows the position where this image was taken from, (b) shows its electron diffraction pattern and (c) shows the TEM image obtained from Sample B. The electron diffraction pattern of Sample B also shows an amorphous nature which is confirmed by its TEM image.

The contrast of the TEM images for amorphous material mainly arises from mass-thickness contrast [3]. The intensities in the TEM images that are not equally distributed may be related to the thickness difference of the specimen.

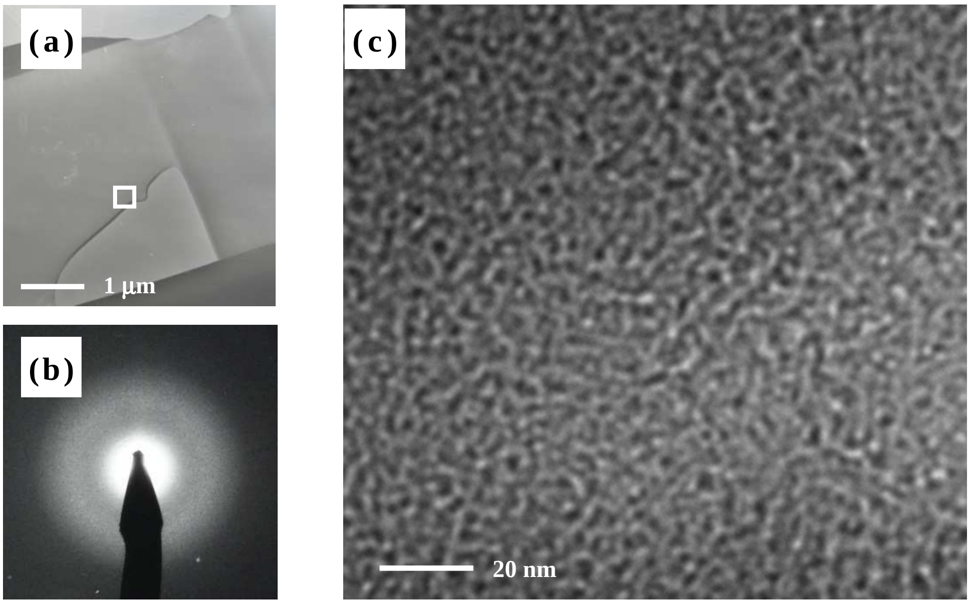

Figure 4.10: (a) the FIB sample image showing where the TEM image was taken, (b) the electron diffraction pattern of Sample A-Green, (c) TEM image of Sample A-Green.

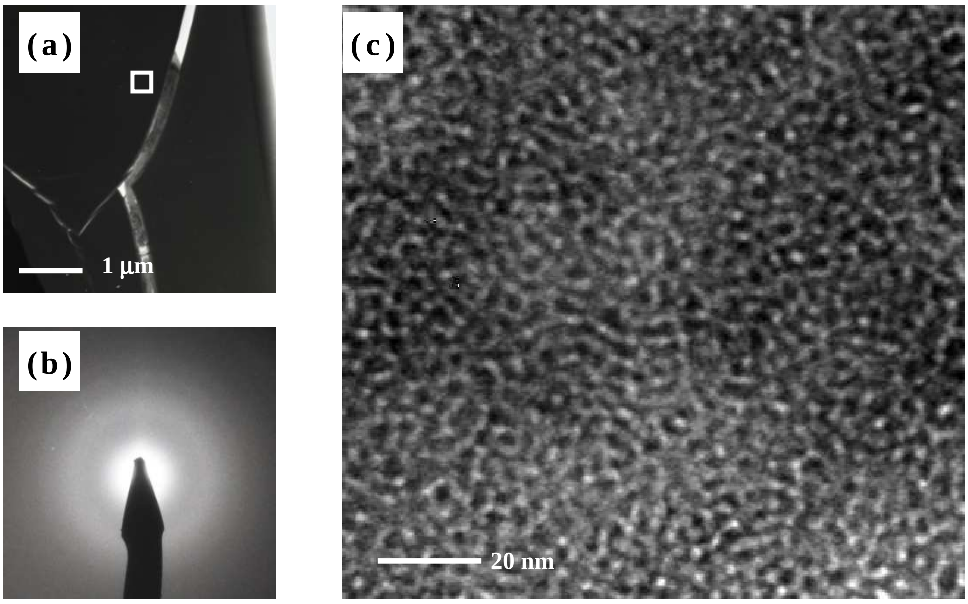

Figure 4.11: (a) the FIB sample image showing where the TEM image was taken, (b) the electron diffraction pattern of Sample A-White, (c) TEM image of Sample A-White.

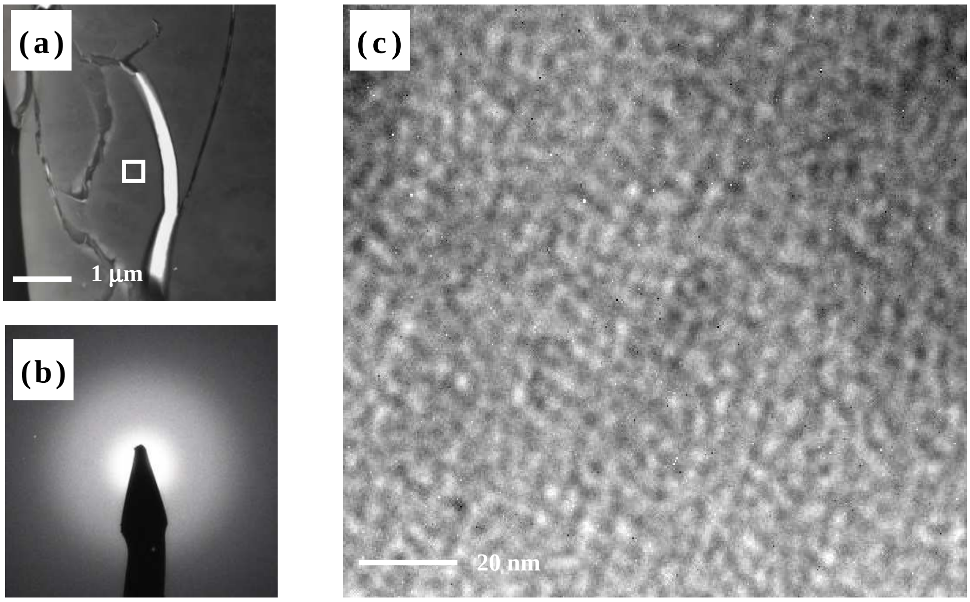

Figure 4.12: (a) the FIB sample image showing where the TEM image was taken, (b) the electron diffraction pattern of Sample B, (c) TEM image of Sample B.

4.1.3.1 Thickness Measurement of TEM Specimens

The effect of specimen thickness on the electron diffraction of amorphous material has been studied in this section. A polycrystalline Al reference sample was used to establish the relationship between the specimen thickness and the Al X-ray intensity collected under a prescribed microscopy condition. The result obtained was compared with the theoretically calculated relationship between the specimen thickness and the Al X-ray intensity and then used as the reference for the later electron diffraction experiments on the amorphous samples.

Convergent beam electron diffraction (CBED) was used to measure the thickness of the Al reference sample. Figure 4.13 shows the CBED pattern obtained from Point 1 at a two-beam condition in Al sample with $\mathbf{g} = (200)$. For Al with lattice parameter of 0.401 nm, the planar spacing of (200) planes is 0.2021 nm, so s_1, s_2, s_3 are given in Table 4.4 as calculated according to formula:

$$s_i = \lambda \frac{\Delta\theta_i}{2\theta_B d^2} \tag{4.1}$$

where λ is the wavelength of electrons equals 0.0025 nm (200kV), $\Delta\theta_i$ is the distance from the mid-line to the chosen minimum and the angle $2\theta_B$ is the separation of the 000 and 200 disks. These values were measured from the CBED pattern shown in Figure 4.13.

The guessed values of n are shown in Table 4.4 (Part A) Column 2, to give the values for $(s_i/n_i)^2$ in Column 3. These data do not plot as a straight line. The integer 2 is then assigned to the first fringe. The second set of values are shown in Table 4.4 (Part B), and a straight line for $(s_i/n_i)^2$ versus $(1/n_i)^2$ was obtained for n = 2 as shown in Figure 4.14. The intercept of the straight line with the ordinate $(s_i/n_i)^2$ is $1/t^2$, and this equals 6.32×10^{-5} nm^{-2}, which results in a foil thickness of t = 125.8 nm.

Table 4.4: thickness determination obtained from Point 1 with different n values: (Part A) n_1=1 and (Part B) n_1=2.

(Part A)

s_i (nm^{-1})	n_i	s_i^2/n_i^2 (nm^{-2})
$s_1 = 0.839 \times 10^{-2}$	1	0.704×10^{-4}
$s_2 = 2.079 \times 10^{-2}$	2	1.081×10^{-4}
$s_3 = 2.956 \times 10^{-2}$	3	0.971×10^{-4}

(Part B)

s_i (nm^{-1})	n_i	s_i^2/n_i^2 (nm^{-2})
$s_1 = 0.839 \times 10^{-2}$	2	0.176×10^{-4}
$s_2 = 2.079 \times 10^{-2}$	3	0.480×10^{-4}
$s_3 = 2.956 \times 10^{-2}$	4	0.546×10^{-4}

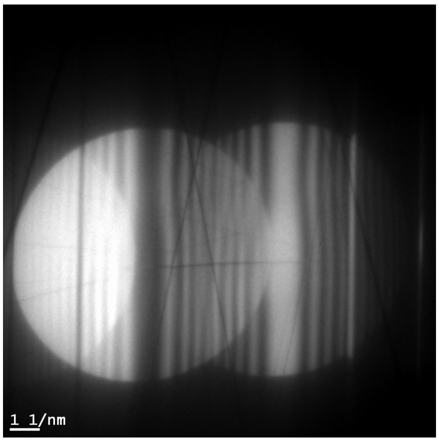

Figure 4.13: CBED pattern in two-beam condition obtained at point 1 with

$\boldsymbol{g} = (200).$

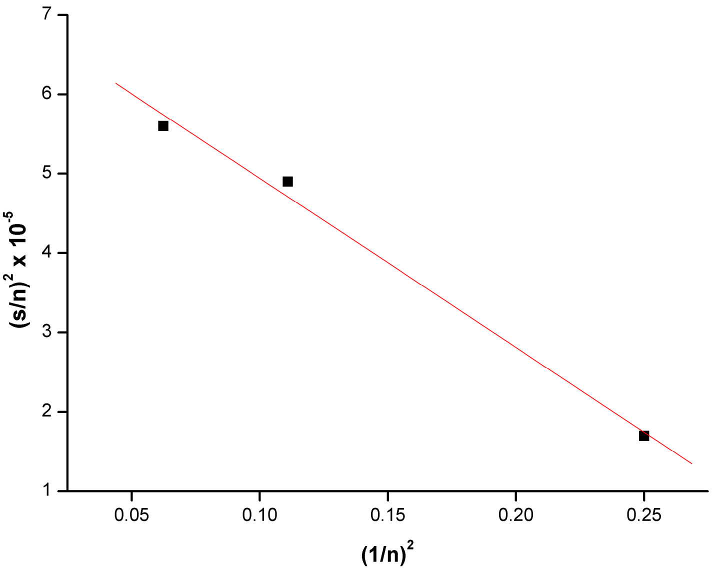

Figure 4.14: a straight line of $(s_i/n_i)^2$ *vs.* $(1/n_i)^2$ *was obtained from Point 1.*

Another two CBED patterns were taken from Point 2 and Point 3 also at a two-beam condition for **g** = 200. Applying the same calculation procedure as shown before, the $(s_i/n_i)^2$ versus $(1/n_i)^2$ profiles for Point 2 and Point 3 can be obtained and shown in Figure 4.15. Figure 4.16 (a) obtained from Point 2 shows that the intercept of the straight line with y-axis at 1.71 x 10^{-5} nm^{-2} which results in a foil thickness of 182.5 nm. Figure 4.16 (b) obtained from Point 3 shows that the intercept of the straight line with y-axis at 10.82 x 10^{-5} nm^{-2}, which results in a foil thickness of 96.2 nm.

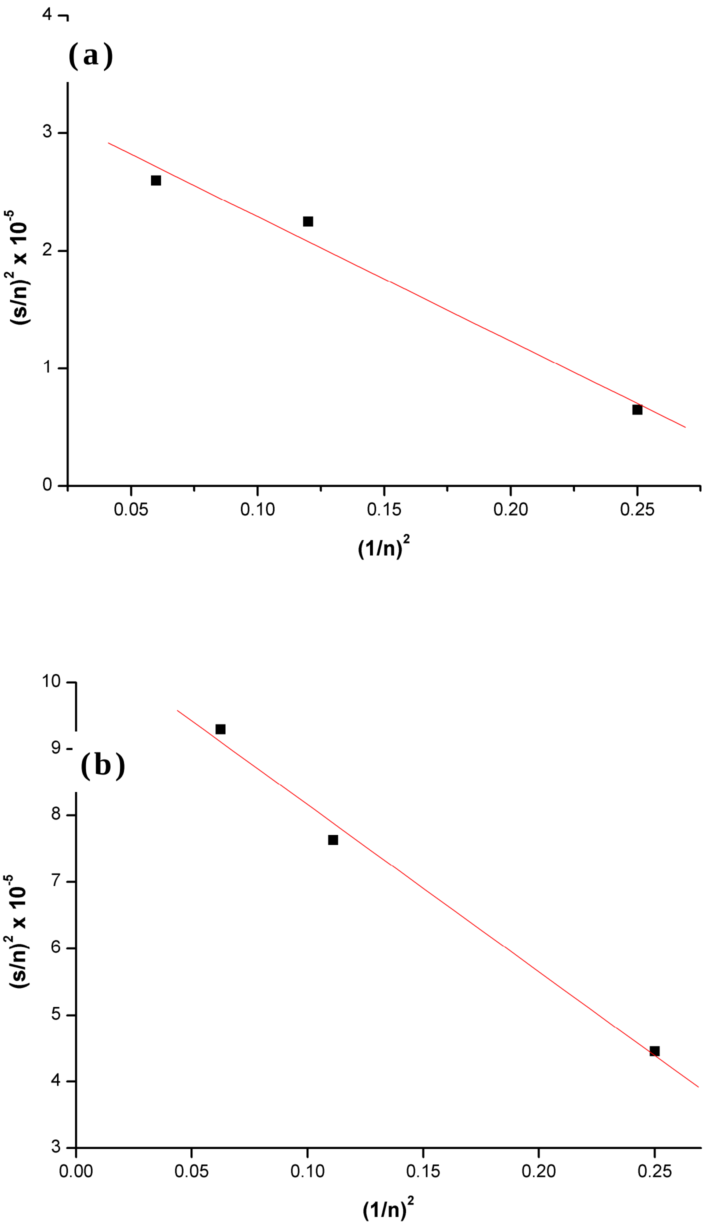

Figure 4.15: the profiles of the straight line of $(s_i/n_i)^2$ *vs.* $(1/n_i)^2$ *obtained from Point 2 (a) and Point 3 (b).*

After the thickness measurement, EDX measurement was performed at the same positions. All EDX measurements were carried out at the same microcopy's conditions, such as accelerating voltage (200 kV), spot size (15 nm) and α-tilt angle (15.9 degrees). The total intensity of the K line characteristic peak of Al was collected from the EDX spectra obtained from Point 1 to 3, as shown in Table 4.5 combined with the thickness measured earlier. Assume the relationship between the Al X-ray intensity and specimen thickness as $I_{Al} = Kt$, where I_{Al} is the measured Al X-ray intensity, t is the specimen thickness with unit of nm and K is a constant. Then the K value K_{exp} can be obtained experimentally as about 789 (nm^{-1}).

Table 4.5: total integral of K line intensity obtained from each point for Al.

Point	Total Counts	Thickness (nm)
1	100099	125.8
2	144622	182.5
3	74766	96.2

On the other hand, the relationship between the characteristic X-ray intensity of a specific element (for example, Al) and the specimen thickness can be theoretically calculated. This is because in TEM thin films, electrons lose only a small fraction of their energy in the film (~5 eV/nm), in addition, few electrons are backscattered. Under these circumstances, the generated characteristic X-ray intensity of Al, I_{Al}^{*} can be given by a simplified formula [5]:

$$I_{Al}^{*} = \frac{KC_{Al}Q_{Al}\omega_{Al}a_{Al}}{A_{Al}}t \qquad \textbf{(4.2)}$$

where K is a material-dependent constant with units (g/cm^3)(atoms/mol) (here assume K equals to $\rho_{Al}N_A$, where ρ_{Al} is the mass density of Al and N_A is the Avogadro number), C_{Al} is the weight fraction of Al (dimensionless), Q_{Al} is the ionization cross section $(cm^2/atom)$, ω_{Al} is the fluorescence yield (ionization fraction resulting in X-ray emission) (dimensionless), a_{Al} is the relative intensity factor (fraction of the total measured K line intensity of Al) (dimensionless), A_{Al} is the atomic weight of Al (g/mol) and t is the thickness of the Al specimen film (membrane) (cm). It should be noted that the ratio K/A_{Al} is a number density (or volume density) with dimensions $(atom/cm^3)$ [5].

Assuming an infinitely thin membrane and neglecting absorption and fluorescence effects, the X-ray intensity generated by the electron beam, I^*_{Al}, should equal the X-ray intensity entering the X-ray detector. However, the measured intensity, I_{Al} on the EDX spectrum is only a small fraction of the generated intensity because the detector size is limited and the generated X-ray intensity may be absorbed as they entering the detector window and the Si detector itself. Thus,

$$I_{Al} = I^*_{Al}\varepsilon_{Al} \qquad \textbf{(4.3)}$$

where ε_{Al} is the detector efficiency for Al [5].

The material-dependent constant K, for Al, equals $\rho_{Al}N_A$ of 16.24×10^{23} (g/cm^3)(atoms/mol). The weight fraction C_{Al} is 1 for a pure Al sample. The ionization cross section Q_{Al} is given as $Q_{Al} = (6.51 \times 10^{-21}/(E_c^2U^{d_s}))n_sb_s\ln|c_sU|$, where n_s is the number of electrons in a shell, b_s and c_s are constants for a particular shell, E_c is the ionization energy of a given shell, $U = (E_0/E_c)$ is the overvoltage, and d_s term that indicates the overvoltage effect that was observed equals $1.0667 - 0.00476(Z)$ (for K lines) [5]. The values used for Al are: $n_s = 2$, $b_s = 1.0269$ [calculated from Ref. [5]], $c_s = 1$, $d_s = 1.00482$, $E_c = 1.560$ keV, $E_0 = 200\text{keV}$. Substituting these values into the equation for Q_{Al} gives: $Q_{Al} = 2.032 \times 10^{-21}$ $(cm^2/atom)$. The fluorescence yield ω_{Al} can be obtained from Ref. [5], by solving the equation $[\omega/(1-\omega)]^{1/4} = A + BZ + CZ^3$, where Z is the atomic number of Al and A, B and C are constants. For a given K line, $A = 0.015$, $B = 0.0327$ and $C = -0.64 \times 10^{-6}$ [5], yields $\omega_{Al} = 0.0357$. The relative intensity factor a_{Al} can be expressed as $a = I_{K_a}/(I_{K_a} + I_{K_\beta})$ [2]. For Al (atomic number is 13), a_{Al} is given as $a_K^{11-19} = 1.052 - 4.39 \times 10^{-4}Z^2$ yields $a_{Al} = 0.978$. A_{Al} is the atomic weight of Al and equals $26.98(g/mol)$. The detector efficiency for Al, ε_{Al}, depends on several microscope-specific parameters [5]. For the instrument Oxford detector on the JEM-2100 used in this study which has a high efficiency for light elements, the value of $\varepsilon_{\mathrm{Al}}$ for K lines taken from Ref [5] $\varepsilon_{\mathrm{Al}} = 0.727$ is used. Substituting the calculated values of K, $\mathrm{C_{Al}}$, $\mathrm{Q_{Al}}$, ω_{Al}, $\mathrm{a_{Al}}$, $\mathrm{A_{Al}}$ and $\varepsilon_{\mathrm{Al}}$ into Eqn. (4.2) and (4.3), the relationship between the Al X-ray characteristic K-line intensity and its specimen thickness can be obtained: $\mathrm{I_{Al}} = 890.01\mathrm{t}$. So the K value established theoretically $\mathrm{K_{Theory}}$ is about 890 ($\mathrm{nm^{-1}}$). Compared with $\mathrm{K_{Theory}}$, the experimental measured value $\mathrm{K_{exp}}$=789 is 12% smaller which is not unreasonable considering the crudity of the estimation. The K value is a material-dependent constant, the different K values for crystalline Al and amorphous Al depends on the mass density of Al.

4.1.3.2 Electron Diffraction Study in TEM

Electron diffraction (ED) technique in TEM is used to characterise the microstructure of the amorphous samples. The high acceleration voltage of TEM allows the fine control over a beam of high energy electrons enabling sophisticated diffraction experiments to be performed. The ED patterns were firstly taken from Sample A with different specimen thickness to study the effect of the specimen thickness on the electron diffraction. ED patterns taken from different samples are studied and the structural information of the samples is obtained by transforming the ED patterns into a reduced density function G(r). This principle has been introduced in Chapter two.

Figure 4.16 shows the electron diffraction patterns taken from Point 1 to 3 (a to c) in Sample A measured at same microscopy conditions. EDX measurements of the specimen thickness were also carried out in Point 1 to 3 and thus the measured thickness of (a) Point 1 is about 133.2 nm, (b) Point 2 is about 159.7 nm and (c) Point 3 is about 195.1 nm. It can be found the patterns show an amorphous nature and the intensities of the diffraction patterns roughly decrease as the specimen thickness increase.

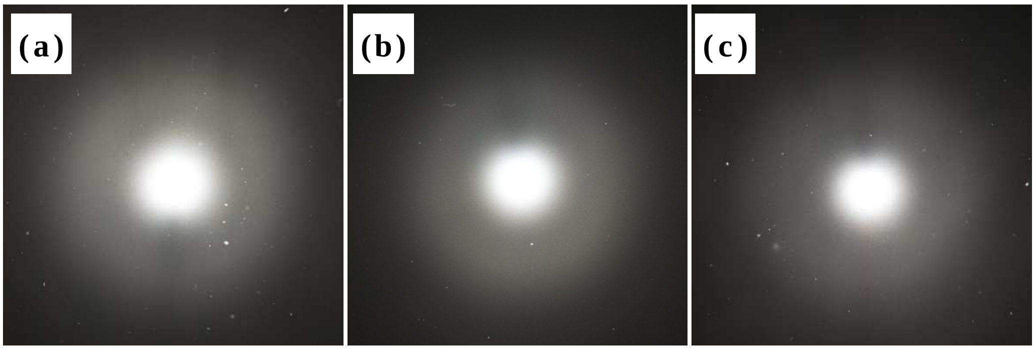

Figure 4.16: electron diffraction patterns taken from: Point 1 (a), Point 2 (b) and Point 3 (c) in Sample A with different thickness.

The next thing is to obtain the structural information from the diffraction patterns. The first step is to obtain the I-R profile, here I refer to the intensity in the diffraction pattern and R is the radius of the ED pattern. Define $\mathbf{Q} = \mathbf{k} - \mathbf{k}'$ where $\mathbf{k}$ and $\mathbf{k}'$ are wave vectors of the incident electron beam and scattered electron beam and $|\mathbf{k}| = \frac{2\pi}{\lambda}$ where λ is the wavelength of the electron. Then:

$$\mathrm{Q} = |\mathbf{Q}| = |\mathbf{k} - \mathbf{k}'| = \frac{4\pi \sin 2\theta}{\lambda} \quad \textbf{(4.4)}$$

where the electron wavelength $\lambda = 0.025\text{Å}$ (200kV), camera length $\mathrm{L} = 60\mathrm{cm}$ and $\sin 2\theta \approx \mathrm{R}/\mathrm{L}$ when $2\theta \to 0$. Then Eqn. (4.5) can be obtained:

$$\mathrm{Q} = \frac{\mathrm{R}}{60}\frac{4\pi}{0.025}. \quad \textbf{(4.5)}$$

Then by transforming the R values into Q values the I-Q profile can be obtained. This I-Q profile is shown for Point 1 to 3 in Figure 4.17. After obtaining the I-Q profile, the next step in calculating G(r) involves converting the intensity I(Q) into $\Phi(\mathrm{Q})$, the reduced intensity function:

$$\Phi(\mathrm{Q}) = \mathrm{Q}\left[\frac{\mathrm{I(Q)} - \mathrm{Nf(Q)}^2}{\mathrm{Nf(Q)}^2}\right]. \quad \textbf{(4.6)}$$

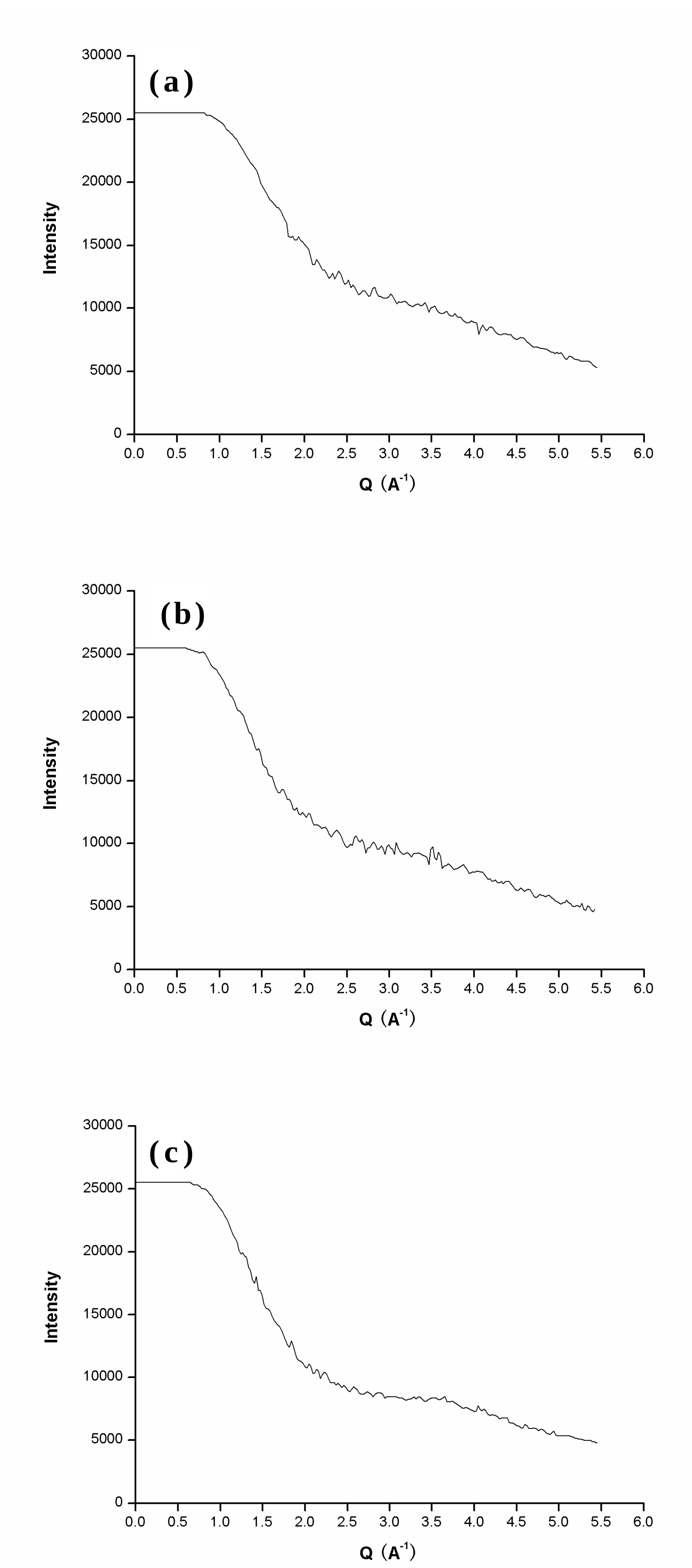

Figure 4.17: I-Q profile obtained from the electron diffraction patterns of Point 1 (a), Point 2 (b) and Point 3 (c) shown in Figure 4.16.

To perform this conversion the values of Nf(Q) at specific Q for a given atom's type need to be known and these values are calculated from tables produced by Doyle and Turner [6] who applied the Born approximation to derive them. Substitute $\mathrm{Nf(Q)} \approx 3780$ into Eqn. (4.6) and $\Phi(\mathrm{Q})$ can be obtained. After obtaining $\Phi(\mathrm{Q})$ from the experimental data now it is possible to calculate G(r) using:

$$\mathrm{G(r)} = \frac{2}{\pi}\int_0^{\infty} \Phi(\mathrm{Q}) \sin(\mathrm{Qr})\, \mathrm{dQ}. \qquad \textbf{(4.7)}$$

In Eqn. (4.7) the integral is performed over all Q from zero to infinity, however, the experimental data is truncated at specific Q values, Q_{min} and Q_{max}, which are normally $0\ \text{Å}^{-1}$ and $10\ \text{Å}^{-1}$. Eqn. (4.8) can then be written as:

$$\mathrm{G(r)} = \frac{2}{\pi}\int_{\mathrm{Qmin}}^{\mathrm{Qmax}} \Phi(\mathrm{Q}) \sin(\mathrm{Qr})\, \mathrm{dQ} \qquad \textbf{(4.8)}$$

Following Eqn. (4.8) the reduced density function G(r) can be obtained for Point 1 to 3 which are shown in Figure 4.18. Figure 4.18 (a) is the G(r) for Point 1, the first three peaks at $\mathrm{r} = 1.51, 2.87$ and 3.98 Å indicate the first, second and third nearest-neighbour distances for Sample A [7]. Figure 4.18 (b) is the G(r) for Point 2, the first three nearest-neighbour distances obtained are 1.51, 2.92 and 4.03 Å. Figure 4.18 (c) is the G(r) for Point 3, the first three nearest-neighbour distances obtained are 1.51, 2.94 and 4.05 Å. The G(r)s for Point 1 to 3 are quite similar, the first nearest-neighbour distance is the same, the second and the third nearest-neighbour distances slightly increase for Point 2 and Point 3. The decrease in the G(r) peak value from Point 1 to 3 may be related to the decrease of the electron diffraction intensity. The thickness change of the specimens thus has no effect on the peak positions in G(r), and the structural information obtained remains the same.

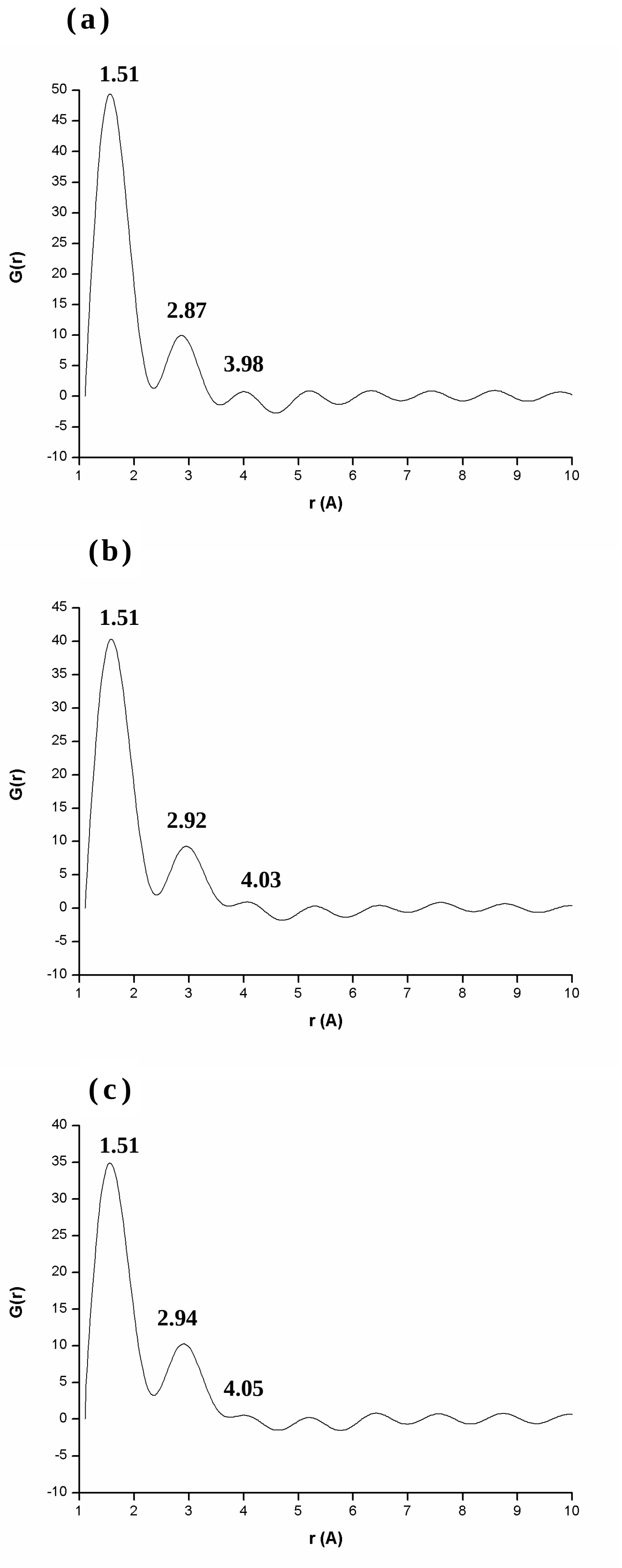

Figure 4.18: reduced density function G(r) obtained from the electron diffraction patterns of Point 1 (a), Point 2 (b) and Point 3 (c) shown in Figure 4.16.

Figure 4.19 shows the electron diffraction patterns taken from Sample A-Green (a), Sample A-White (b) and Sample B (c). They all indicate the amorphous nature of the samples because a diffuse but distinct halo on a steadily falling background can be observed in the diffraction pattern. Applying the same calculation procedures which were shown before, the reduced density function G(r) can be obtained for the samples which is shown in Figure 4.20.

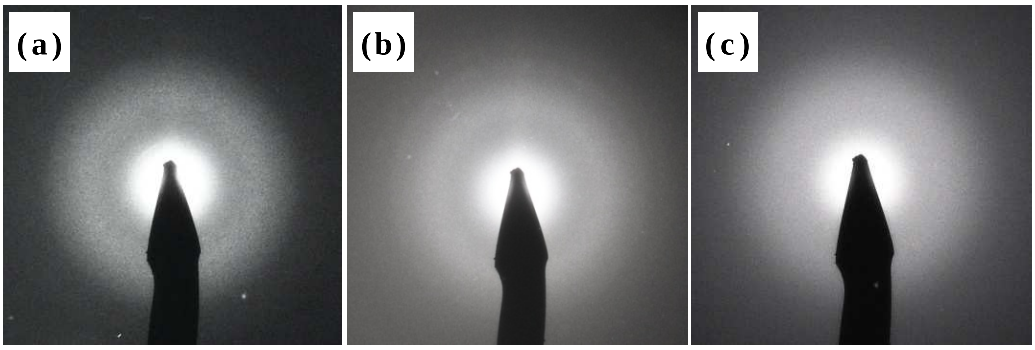

Figure 4.19: electron diffraction patterns taken from: Sample A-Green (a), Sample A-White (b) and Sample B (c).

Figure 4.20 shows the G(r)s for Sample A-Green (a), Sample A-White (b) and Sample B (c). Figure 4.20 (a) indicates the first three nearest-neighbour distances for Sample A-Green at $r = 1.51, 2.87 \text{ and } 3.98\,\text{Å}$. Figure 4.20 (b) indicates the first three nearest-neighbour distances for Sample A-White obtained at 1.48, 2.83 and 3.92 Å. The value of the first nearest-neighbour distances for Sample A-White is slightly lower than Sample A-Green. Figure 4.20 (c) indicates the first three nearest-neighbour distances for Sample B obtained at 1.71, 3.01 and 4.12 Å. Compare with Sample A-Green and Sample A-White, Sample B has relatively larger first nearest-neighbour distance.

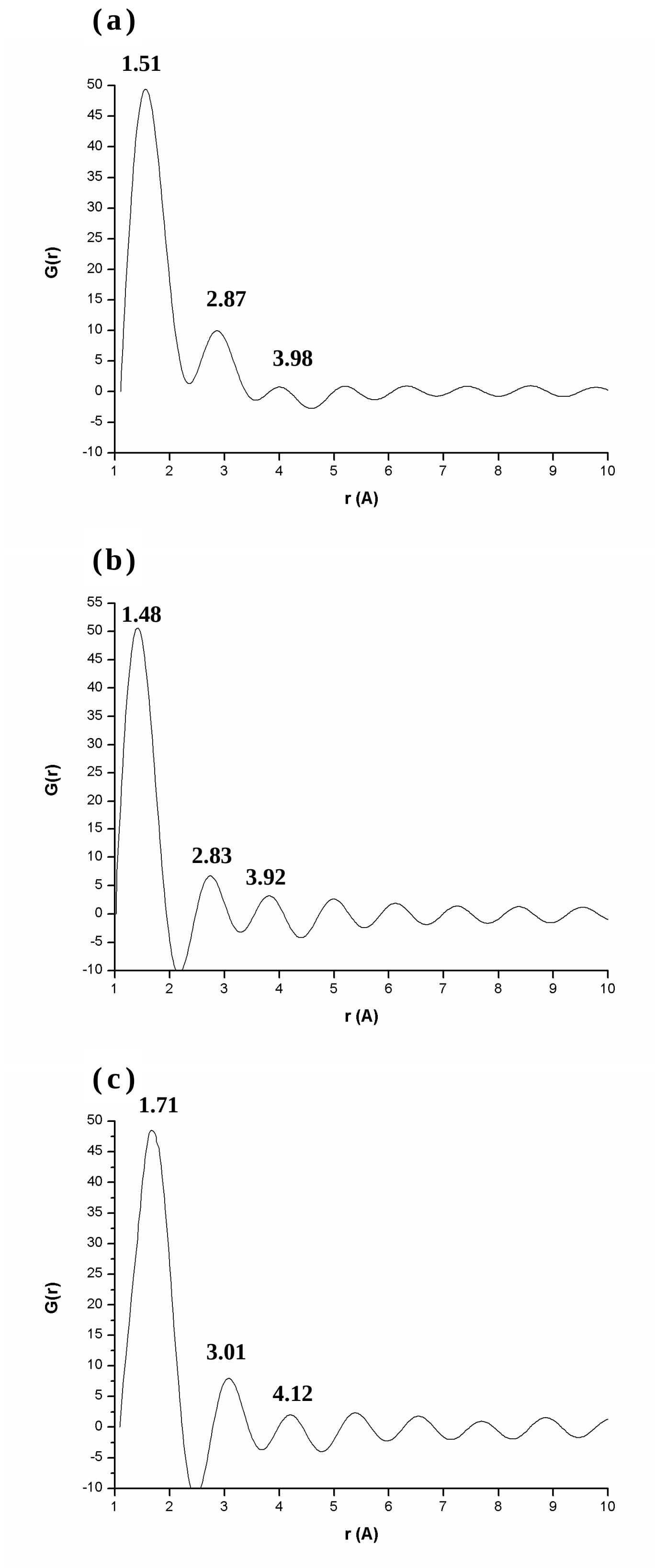

Figure 4.20: reduced density function G(r) obtained from the electron diffraction patterns of Sample A-Green (a), Sample A-White (b) and Sample B (c) shown in Figure 4.19.

4.2 Mechanical Properties

4.2.1 Vickers Hardness

Table 4.6 shows the summary of Vickers hardness results of Sample A-Green, Sample A-White and Sample B. The values for each sample were obtained from an average of six measurements and with fairly constant results. Sample A has relatively higher hardness value than Sample B.

Table 4.6: the summary of Vickers hardness results.

	Average (HV)	**Std. Deviation (HV)**
Sample A-Green	714.3	15.8
Sample A-White	725.5	16.4
Sample B	589.7	18.9

4.2.2 Compression Test

Table 4.7 shows the summary of compression test results including the maximum force, the break force and the contact area. The compressive strength of Sample A is higher than the compressive strength of Sample B. Figure 4.21 demonstrates the stress-strain curve of the compression test for Sample A and Sample B.

The difference of Vickers Hardness and compressive strength for Sample A and Sample B may be related to its microstructure diffenence. Due to the previous study, Sample A has smaller first nearest-neighbour distance than Sample B, and the black fiber like structure which can be found in Sample B do not exist in Sample A.

Table 4.7: the summary of compression test results.

	F_{max} (N)	**F_{break} (N)**	**S_0 (mm$^{2)}$**	**Compressive Strength (MPa)**
Sample A	28805.00	27637.62	39.59	727.58
Sample B	16063.56	14228.11	27.38	529.65

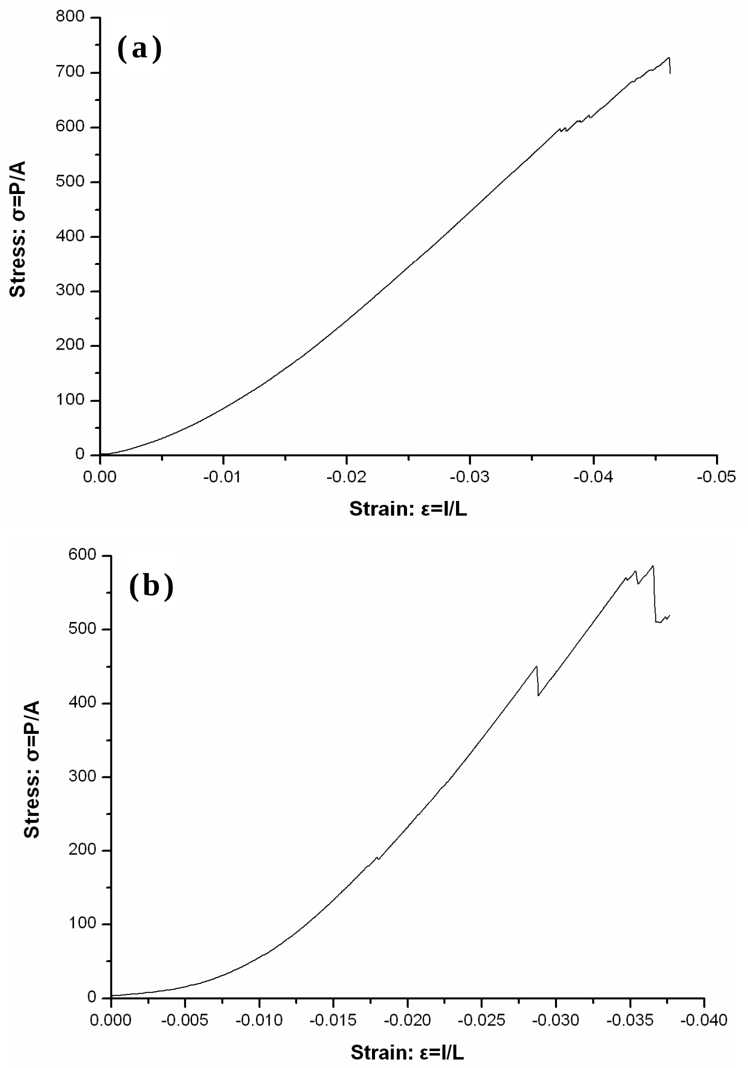

Figure 4.21: stress-strain curves of Sample A (a) and Sample B (b).

4.3 Chemical Stability

4.3.1 Dissolution in Alkaline Solution

The dissolution behaviour of the samples was studied in this section by dissolving the waste glass in alkaline solutions. Alkaline solutions were prepared by dissolving analytical reagent-grade sodium hydroxide in distilled water. Sample was immersed in alkaline solution for various times, and the weight loss of the sample was measured every 4 hours in the first 2 days and then every 12 hours for another 12 days. The samples and alkaline solutions used were shown in Table 4.7

Table 4.8: samples and alkaline solutions used in dissolution experiment.

Samples	**From**	**NaOH Solution (concentration)**
A-1	Sample A	0.01 mol/dm^{-3}
A-2	Sample A	0.02 mol/dm^{-3}
A-3	Sample A	0.05 mol/dm^{-3}
A-4	Sample A	0.1 mol/dm^{-3}
B-1	Sample B	0.01 mol/dm^{-3}
B-2	Sample B	0.02 mol/dm^{-3}
B-3	Sample B	0.05 mol/dm^{-3}
B-4	Sample B	0.1 mol/dm^{-3}

Figure 4.22 shows the dissolution profiles (weight loss versus time) of Sample A (A-1 to A-4) and Sample B (B-1 to B-4) in alkaline solutions with different concentrations. The rate of the weight loss increases with the concentration of the alkaline solution both for Sample A and Sample B. When the alkaline solution's concentration is 0.01 mol/dm^{-3}, after 336 hours, the weight loss of A-1 is about 0.027 g and for B-1 is about 0.021 g. When the alkaline solutions concentration increases to 0.02 mol/dm^{-3}, 0.05 mol/dm^{-3} and 0.1 mol/dm^{-3} respectively after 336 hours, the weight loss of A2 to A-4 increase to about 0.045 g, 0.057g and 0.095 g respectively; the weight loss of B-2 to B-4 increase to about 0.034g, 0.049g and 0.079g respectively. Compare with Sample B, Sample A has higher dissolution rate under the same conditions. This may be related to the different chemical compositions and microstructure of Sample A and Sample B which is indicated in previous SEM and TEM studies.

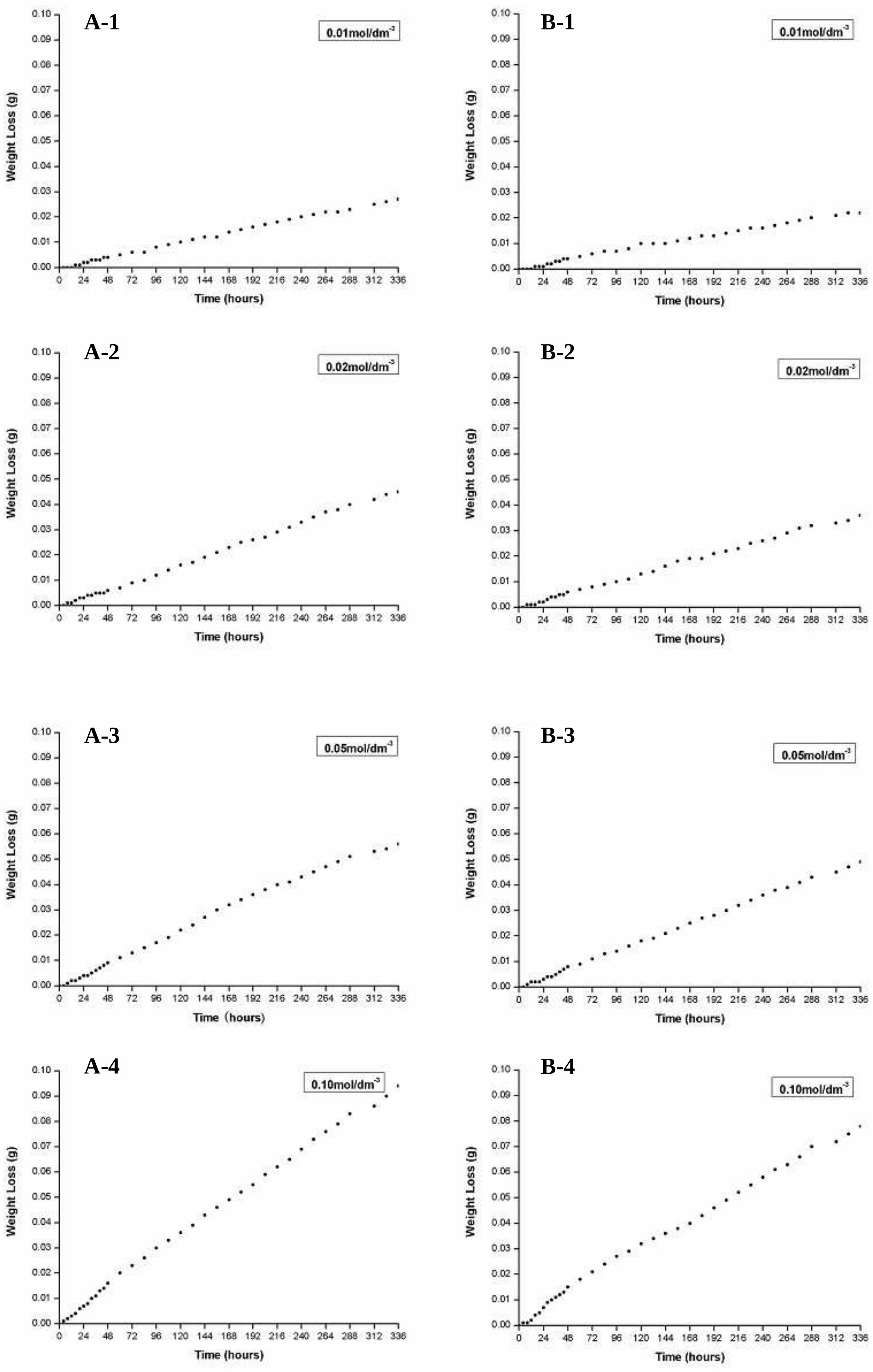

Figure 4.22: dissolution profiles (weight loss vs. time) of Sample A (A-1 to A-4) and Sample B (B-1 to B-4) in alkaline solutions of different concentrations.

References

[1] M. Imaoka, H. Hasegawa, I. Yasui, Phys. Chem. Glasses 24 (1983) 72.

[2] N. Aoki, H. Hasegawa, I. Yasui, Yogyo Kyokaishi 94 (1986) 539.

[3] D. Brandon, W. D. Kaplan, *Microstructural Characterization of Materials*, John Wiley & Sons, 2008.

[4] A.J. Wilkinson, P.B. Hirsch, Micron 28 (1997) 279.

[5] D. C. Joy, A. D. Romig, Jr., J. I. Goldstein (Ed), Principles of Analytical Electron Microscopy, 1986, Plenum, New York.

[6] P. A. Doyle, P. S. Turner, Acta Cryst. 24 (1968) 390.

[7] H. Hirai, Y. Tabira, K. Kondo, T. Oikawa, N. Ishizawa, Phys. Rev. B 52 (1995) 9.

CHAPTER FIVE

CONCLUSIONS

Based on the present study, the following conclusions can be drawn:

1. Both the sodium-free sample and the sodium-containing sample are amorphous; this is confirmed by the XRD and electron diffraction studies.

2. The green area in sodium-free sample has a homogeneous structure and the white area has a dendrite-like structure, containing a bright part with more Al, Si, Ce but less Mg than the dark part. A black fiber-like structure can be found in the sodium-containing sample and contains more O, Mg, Al but less Si than other part in the sample. TEM result shows that this black fiber-like structure is also amorphous.

3. TEM electron diffraction study shows that sodium-containing sample has a larger nearest-neighbor distance than the sodium-free sample and this is revealed by the reduced density function G(r). The effect of the specimen thickness on electron diffraction was performed. It is found that when the thickness of specimen increases, the peak positions in the G(r) profile remain the same, the thickness of specimen has no effect on the electron diffraction.

4. The sodium-free sample has a higher Vickers hardness (714.3 ± 15.8 HV) than the sodium-containing sample (589.7 ± 18.9 HV). The sodium-free sample also has a higher compressive strength (727.6 MPa) than the sodium-containing sample (529.7 MPa).

5. The dissolution rate of the sodium-free and the sodium-containing samples increases with the concentration of the alkaline solution. The sodium-free sample

has higher dissolution rate than the sodium-containing sample under the same conditions.

Appendix

A. 1 Fourier Transform

A function such like the electron wavefunction can be described by its real-space representation $\psi(\mathbf{r})$, or in reciprocal space by its Fourier transform $\emptyset(\mathbf{q})$. The two forms $\psi(\mathbf{r})$ and $\emptyset(\mathbf{q})$ are two different representations of the same physical function. These two representations can be transformed by means of the integral transformations:

$$\psi(\mathbf{r}) = (2\pi)^{-3}\int \emptyset(\mathbf{q})e^{i\mathbf{q}.\mathbf{r}}d\mathbf{q}$$

$$\emptyset(\mathbf{q}) = \int \psi(\mathbf{r})e^{-i\mathbf{q}.\mathbf{r}}d\mathbf{r}$$

where the integral signs imply integration over the whole spaces of the vectors $\mathbf{q}$ and $\mathbf{r}$.

A. 2 The Dirac Delta Function

The Dirac delta function is defined by the equations:

$$\delta(\mathbf{r}) = 0, \text{if } \mathbf{r} \neq 0$$

$$\int \delta(\mathbf{r})d\mathbf{r} = 1$$

The Dirac delta function is not an ordinary mathematical function, actually this function has meaning only if it is used as an argument of an integral, i.e.:

$$\int \delta(\mathbf{r}-\mathbf{a})f(\mathbf{r})d\mathbf{r} = f(\mathbf{a})$$

It is often convenient to express the Dirac delta function in terms of its Fourier transform:

$$\delta(\mathbf{r}) = (2\pi)^{-3} \int e^{\mathbf{iq.r}} d\mathbf{q}$$

Alternatively in reciprocal space:

$$(2\pi)^3 \delta(\mathbf{k}) = \int e^{-\mathbf{ik.r}} d\mathbf{r}.$$

List of Tables

List of Figures

Figure 4.7: (a) TEM image of Sample B showing the existence of the black fiber-like structure and (b) electron diffraction pattern performed at the black fiber-like structure show (b) an amorphous structure.

Figure 4.8: image showing where the line scan was performed.

Figure 4.9: line scan profiles performed through the black fiber-like structure: (a) is the profile with concentration scale 0 to 80 (at.%) and (b) is the same profile with concentration scale 0 to 5 (at.%).

Figure 4.10: (a) the FIB sample image showing where the TEM image was taken, (b) the electron diffraction pattern of Sample A-Green, (c) TEM image of Sample A-Green.

Figure 4.11: (a) the FIB sample image showing where the TEM image was taken, (b) the electron diffraction pattern of Sample A-White, (c) TEM image of Sample A-White.

Figure 4.12: (a) the FIB sample image showing where the TEM image was taken, (b) the electron diffraction pattern of Sample B, (c) TEM image of Sample B.

Figure 4.13: CBED pattern in two-beam condition obtained at point 1 with $\mathbf{g} = (200)$.

Figure 4.14: a straight line of $(s_i/n_i)^2$ vs. $(1/n_i)^2$ was obtained from Point 1.

Figure 4.15: the profiles of the straight line of $(s_i/n_i)^2$ vs. $(1/n_i)^2$ obtained from Point 2 (a) and Point 3 (b).

Figure 4.16: electron diffraction patterns taken from: Point 1 (a), Point 2 (b) and Point 3 (c) in Sample A with different thickness.

Figure 4.17: I-Q profile obtained from the electron diffraction patterns of Point 1 (a), Point 2 (b) and Point 3 (c) shown in Figure 4.16.

Figure 4.18: reduced density function G(r) obtained from the electron diffraction patterns of Point 1 (a), Point 2 (b) and Point 3 (c) shown in Figure 4.16.

Figure 4.19: electron diffraction patterns taken from: Sample A-Green (a), Sample A-White (b) and Sample B.

Figure 4.20: reduced density function G(r) obtained from the electron diffraction patterns of Sample A-Green (a), Sample A-White (b) and Sample B (c) shown in Figure 4.19.

Figure 4.21: stress-strain curves of Sample A (a) and Sample B (b).

Figure 4.22: dissolution profiles (weight loss vs. time) of Sample A (A-1 to A-4) and Sample B (B-1 to B-4) in alkaline solutions of different concentrations.